

Joint-Scatterer Processing for Time-Series InSAR

Xiaolei Lv, *Member, IEEE*, Birsen Yazıcı, Mourad Zeghal, Victoria Bennett, and Tarek Abdoun

Abstract—The first-generation time-series synthetic aperture radar interferometry (TSInSAR) technique persistent-scatterer (PS) InSAR has been proven effective in ground deformation measurement over areas with high reflectivity by taking advantage of coregistered temporally coherent pointwise scatterers. In order to increase the spatial density of measurement points and quality of displacement time series over moderate reflectivity scenes, a second-generation TSInSAR called SqueeSAR was developed to extract displacement information from both PSs and distributed scatterers, by taking into account their temporal coherence and their spatial statistical behavior. In this paper, we propose a new second-generation TSInSAR, which is referred to as joint-scatterer (JS) InSAR, to measure the line-of-sight surface displacement using the neighboring pixel stacks. A novel goodness-of-fit testing approach is proposed to analyze the similarity between two JS vectors based on time-series likelihood ratios. By taking advantage of the proposed test, a new spatially adaptive filter is developed to estimate the covariance matrix. Based on the estimated covariance matrix, the projection of the joint signal subspace onto the corresponding joint noise subspace is applied to retrieve phase history. With coherence information of neighboring pixel stacks, JSInSAR is able to provide reliable geophysical parameters in the presence of large coregistration errors. The effectiveness of the proposed technique is verified with a time series of high-resolution SAR data from the TerraSAR-X satellite.

Index Terms—Covariance matrix, goodness-of-fit test, joint scatterers, likelihood ratios, persistent scatterers, SAR interferometry (InSAR), spatially adaptive filter, SqueeSAR, synthetic aperture radar (SAR).

I. INTRODUCTION

SYNTHETIC aperture radar interferometry (InSAR) is a remote sensing technique that offers the capability for recovering fine-resolution topographic profiles and measuring possible displacements of radar targets along the line of sight (LOS). In the past two decades, significant progress has been

made in the use of InSAR measurement and monitoring deformation of the Earth's surface, including volcanic activity [1]–[3], seismic-related events [4], [5], landslides [6], glacier motion [7], [8], and urban subsidence [9]. The first successful InSAR technique applied in detecting various surface deformation is referred to as differential InSAR (DInSAR) [7], [10], which subtracts topographic contribution from the differential phase values of two SAR scenes collected at different times over the same area of interest. However, DInSAR usually suffers from temporal and geometrical decorrelation due to reflectivity changes and atmospheric effects due to time-varying tropospheric and ionospheric conditions [7]. In order to overcome these limitations, several techniques have been proposed, such as persistent-scatterer (PS) InSAR (PSI) [11], [12], differential SAR tomography [13], and a small baseline subset (SBAS) technique [14]. The PSI only considers the PSs to minimize the phase dispersions and the consequent loss of coherence. Since the PSs are unaffected by temporal and geometrical decorrelation, all combinations are employed in the PSI method, even those that exceed the critical baseline. However, the major drawback of PSI is the possible low spatial density of measurement points due to the lack of dominant scatterers in the radar target region of interest. The SBAS method exploits an appropriate combination of differential interferograms produced by SAR image pairs characterized by a small orbital separation to limit the spatial decorrelation effects. It has been successfully applied to investigate volcanic and tectonic deformation [15], [16]. Although the applied small baseline constrains the selected SAR image pairs, the density of coherent pixels is typically not homogeneous in the scene, and the spatially dense results are typically limited to mostly in urban and rocky areas, where decoorrelation has a limited impact [17]. In [18], a new algorithm that combines both PS and SBAS approaches was proposed to maximize the spatial sampling of usable signals. In order to increase the density of measurement points in nonurban areas, the latest time-series InSAR technique (TSInSAR) referred to as SqueeSAR was proposed in 2011 [19] to extract deformation from both PSs and statistically homogeneous distributed scatterers (DSs) by applying a spatially adaptive filter and the maximum-likelihood technique.

Extracting deformation from DSs is extremely important in some natural hazard applications. Taking a global assessment of levee failure hazard for an example, the classic PSI technique fails to provide qualified measurement points for the needs of the health assessment framework since the majority of levees in the world are covered by grass. In this paper, a novel DS analysis technique, termed as joint-scatterer InSAR (JSInSAR), is proposed to improve the temporal coherence of DSs by jointly processing neighboring pixel stacks. The idea of JS processing comes from [20], where the coherent information

Manuscript received March 18, 2013; revised August 30, 2013 and January 9, 2014; accepted January 29, 2014. Date of publication April 21, 2014; date of current version May 30, 2014. This work was supported in part by the National Institute of Standards and Technology through the Technology Innovation Program under Cooperative Agreement 70NANB10H018. The work of B. Yazıcı was supported by the U.S. National Science Foundation under Grant CCF-1218805. The work of X. Lv was supported in part by the Hundred Talents Program under Grant Y3Z0110244.

X. Lv was with the Department of Civil and Environmental Engineering, Rensselaer Polytechnic Institute, Troy, NY 12180-3590 USA. He is now with the Institute of Electronics, Chinese Academy of Sciences, Beijing 100190, China (e-mail: blue_horse@163.com).

B. Yazıcı is with the Department of Electrical, Computer, and System Engineering and the Department of Biomedical Engineering, Rensselaer Polytechnic Institute, Troy, NY 12180 USA (e-mail: yazici@ecse.rpi.edu).

M. Zeghal, V. Bennett, and T. Abdoun are with the Department of Civil and Environmental Engineering, Rensselaer Polytechnic Institute, Troy, NY 12180-3590 USA (e-mail: zeghal@rpi.edu; bennev@rpi.edu; about@rpi.edu).

Color versions of one or more of the figures in this paper are available online at <http://ieeexplore.ieee.org>.

Digital Object Identifier 10.1109/TGRS.2014.2309346

of neighboring pixel pairs was exploited to coregister automatically two SAR images and estimate the corresponding interferometric phase. One advantage of JS processing over traditional single-scatterer processing lies in the capability of accurate retrieval of interferometric phase even in the presence of large coregistration errors. In other words, the proposed JSInSAR technique does not strongly rely on the assumption that a set of SAR images are properly coregistered on the same master grid. Another advantage of JS processing is that it allows for the combination of time series of statistically homogeneous patches to get better temporal coherence in comparison with SqueeSAR. The physical justification for the second advantage is that a large set of pixels can be combined and incorporated to increase the SNR since the patch-based filter can be considered nonlocal. Such patch-based filters or estimators have been popularly used in the InSAR community recently (e.g., see [21], [22]). However, the selection of patches may be subject to the topographic relief, which will be discussed later.

Prior to jointly processing neighboring pixel stacks, a test statistic to analyze the similarity between two JS vectors is required. Although many powerful goodness-of-fit testing approaches exist, including the Kullback–Leibler divergence, the Kolmogorov–Smirnov (KS) test, the Anderson–Darling test, and the generalized likelihood ratio (GLR) test, they fail to discriminate between the different amplitude distributions since the similarity analysis between two JS vectors is more than 1-D testing. In this paper, a new goodness-of-fit testing approach, termed as the time-series likelihood ratio (TSLR) test, is proposed, which considers the maximum value of a set of likelihood ratios from time-series patch pairs as a measure of misfit. Based on the proposed test, a new spatially adaptive filter, referred to as the JS filter, is developed to identify the statistically homogeneous joint data vectors and estimate the corresponding covariance matrix.

Using the estimated covariance matrix, the joint subspace projection (JSP) that is an extension of the original one in [20] is exploited to retrieve the optimal interferometric-phase time series. An example of JSP applied in TSInSAR can be found in [23]. The principle of JSP is based on the projection of the joint signal subspace onto the corresponding joint noise subspace by making use of the coherent information of neighboring pixel stacks. Similar to the framework of SqueeSAR, the original data set can be preprocessed by applying the proposed filter and the JSP algorithm, and both PSs and DSs can be simultaneously processed by the standard PSI technique. Therefore, the proposed JSInSAR is completed without the need of significant changes to the classic PSI processing chain.

This paper is organized as follows. Section II introduces the concept of JS vector and pixel stack. Section III proposes a novel goodness-of-fit test, analyzes the similarity based on different amplitude distributions, and then develops the corresponding adaptive filter. Section IV presents the JSP algorithm applied to the case of TSInSAR and analyzes its robustness with respect to coregistration errors. The procedure of the proposed JSInSAR is described in the end of Section IV. In Section V, the performance of JSInSAR, including the increased spatial density, quality improvement, and the robustness relative to coregistration errors are analyzed and validated by using 42

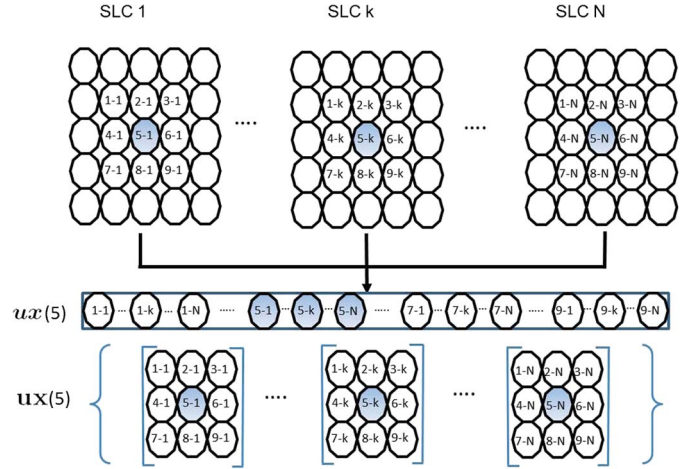


Fig. 1. Formulation of JS vector with a window of 3×3 .

TerraSAR-X high-resolution data acquired from New Orleans, LA, USA. Section VI concludes this paper.

II. SIGNAL MODEL

In this paper, the boldface, boldface italics, and Roman lowercase letters are used to denote matrix, vector, and scalar variables, respectively.

Given a stack of N single-look complex (SLC) SAR images, which is assumed properly coregistered, the joint data vector $\mathbf{u}\mathbf{x}$ can be formulated as

$$\mathbf{u}\mathbf{x}(m) = \left[\mathbf{x} \left(m - \frac{k_1 \times k_2 - 1}{2} \right)^T, \dots, \mathbf{x}(m)^T, \dots, \mathbf{x} \left(m + \frac{k_1 \times k_2 - 1}{2} \right)^T \right]^T \quad (1)$$

where superscript T denotes vector transpose; k_1 and k_2 are the sizes of a window and assumed to be odd numbers; $\mathbf{x}(i)$, $i \in [m - (k_1 \times k_2 - 1)/2, m + (k_1 \times k_2 - 1)/2]$, is referred to as a pixel stack (corresponding to the same ground resolution cell), i.e., $\mathbf{x}(i) = [x_{11}(i), \dots, x_{N1}(i)]$ with $x_j(i)$, $1 \leq j \leq N$, denoting the i th pixel in j th SLC; and $\mathbf{x}(m)$ is the desired pixel stack whose phase vector needs to be retrieved. To better understand the concept of JSs, an example to formulate the joint data vector is shown in Fig. 1, where a 3×3 window centered at the blue circle contains nine pixels in each image, and the blue circles represent the desired pixel stack. Let $k' = (k_1 \times k_2 - 1)/2$. Joint data vector $\mathbf{u}\mathbf{x}$ can be written as [24]

$$\mathbf{u}\mathbf{x}(m) = \mathbf{a}(\phi_{m-k'}, \dots, \phi_m, \dots, \phi_{m+k'}) \odot \mathbf{u}\mathbf{s}(m) + \mathbf{u}\mathbf{w}(m) \quad (2)$$

$$\mathbf{a}(\phi_{m-k'}, \dots, \phi_m, \dots, \phi_{m+k'}) = [\mathbf{a}^T(\phi_{m-k'}), \dots, \mathbf{a}^T(\phi_m), \dots, \mathbf{a}^T(\phi_{m+k'})]^T \quad (3)$$

where \odot denotes the Hadamard product, $\mathbf{a}(\phi_{m-k'}) = \dots = \mathbf{a}(\phi_m) = \dots = \mathbf{a}(\phi_{m+k'}) = \exp(j\phi_m)$ with $\phi_m = [\vartheta_1, \vartheta_2, \dots, \vartheta_N]$ is called the spatial steering vector of the pixel stack $\mathbf{x}(m)$, ϕ_m is the interferometric phase to be estimated, $\mathbf{u}\mathbf{s}(m)$ is the complex reflectivity vector, and $\mathbf{u}\mathbf{w}(m)$ is the additive noise assumed mutually independent spatially white complex Gaussian distributed with zero mean and variance $\sigma_{\mathbf{u}\mathbf{w}}^2$. In (1), the complex

joint data vector can be modeled as a joint zero-mean complex circular Gaussian random vector under the Gaussian scattering assumption based on the central limit theorem [25]. Denoting by $\mathbf{u}\mathbf{a}(\phi_m) = \mathbf{a}(\phi_{m-k'}, \dots, \phi_m, \dots, \phi_{m+k'})$, the corresponding covariance matrix $\mathbf{C}_{\mathbf{u}\mathbf{x}}(m)$ is given by

$$\begin{aligned} \mathbf{C}_{\mathbf{u}\mathbf{x}}(m) &= E \{ \mathbf{u}\mathbf{x}(m) \mathbf{u}\mathbf{x}^H(m) \} \\ &= \mathbf{u}\mathbf{a}(\phi_m) \mathbf{u}\mathbf{a}^H(\phi_m) \odot \mathbf{R}_{\mathbf{u}\mathbf{s}}(m) + \sigma_{\mathbf{u}\mathbf{w}}^2 \mathbf{I}. \end{aligned} \quad (4)$$

where superscript H denotes vector conjugate transpose, $\mathbf{R}_{\mathbf{u}\mathbf{s}}(m)$ is the correlation coefficient matrix that only contains the signal components and is written as

$$\mathbf{R}_{\mathbf{u}\mathbf{s}}(m) = \begin{bmatrix} \mathbf{R}_{\mathbf{s}}(m-k') & 0 & \cdots & 0 \\ 0 & \mathbf{R}_{\mathbf{s}}(m-k'+1) & & \\ \vdots & & \ddots & \\ 0 & & & \mathbf{R}_{\mathbf{s}}(m+k') \end{bmatrix}$$

with

$$\mathbf{R}_{\mathbf{s}}(m) = \begin{bmatrix} r_{11}(m) & \cdots & r_{1N}(m) \\ & \ddots & \\ r_{N1}(m) & \cdots & r_{NN}(m) \end{bmatrix}$$

and $r_{ij}(m)$ denotes the correlation coefficient of the pixel pair m between SLCs i and j .

Using the signal model of joint pixel stacks and the corresponding covariance matrix, a new adaptive filter and a phase history retrieval algorithm used in JSInSAR will be introduced in the following.

III. SPATIALLY ADAPTIVE FILTERING

In practice, the actual covariance matrix in (4) is not known. The most classic and simplest estimator of a covariance matrix is the sample covariance matrix obtained from a sample of the independent and identically distributed (i.i.d.) or statistically homogeneous joint data vectors. The goal of this section is to determine which of the JS vectors presents a similar statistical behavior for each desired pixel stack and to get an estimated covariance matrix. A new goodness-of-fit approach, termed as the TSLR test, is proposed to analyze the similarity between two JS vectors and a new adaptive filter, which is referred to as JS filter, is then developed to estimate the covariance matrix.

A. Patch Similarity Criteria

As shown in Fig. 1, the joint data vector $\mathbf{u}\mathbf{x}(m)$ is a stack of N patches, and each patch is a collection of $k_1 \times k_2$ observations (complex pixel values). We reformulate $\mathbf{u}\mathbf{x}(m)$ as a $k_1 \times k_2 \times N$ 3-D matrix, i.e.,

$$\mathbf{u}\mathbf{x}(m) = [\mathbf{x}_1(m), \dots, \mathbf{x}_N(m)] \quad (5)$$

where $\mathbf{x}_i(m)$ denotes a patch centered at the m th pixel in the i th SLC. Given two data matrices $\mathbf{u}\mathbf{x}(m_1)$ and $\mathbf{u}\mathbf{x}(m_2)$, the two joint data vectors centered at m_1 and m_2 are statistically homogeneous if the null hypothesis that the two matrices are drawn from the same probability distribution function (pdf) is accepted under a certain similarity criterion. From (5), we can see that the similarity analysis between two JS vectors is

a multidimensional goodness-of-fit test. For the 1-D case, the most widely used in SAR is the two-sample KS test [26], [27], which considers simply the maximum distance between the cumulative distribution functions (cdfs) as a measure of misfit. However, this type of test and its variants fail to work in higher dimensions since the corresponding straightforward extensions to more than one dimension are not distribution free and no universal significance levels can be established [28]. It is noted from (5) that the similarity between two patches coming from their respective joint data vectors should be detected prior to judging if $\mathbf{u}\mathbf{x}(m_1)$ and $\mathbf{u}\mathbf{x}(m_2)$ are statistically homogeneous. In the remainder of this paper, we denote the pdf by $p(\cdot)$, and m in (5) will be ignored for ease of readability.

Let us consider two noisy patches denoted by $\mathbf{x}_{1,j}$ and $\mathbf{x}_{2,j}$ from the same SLC j . The pair of noisy patches $(\mathbf{x}_{1,j}, \mathbf{x}_{2,j})$ is similar when $\mathbf{x}_{1,j}$ and $\mathbf{x}_{2,j}$ are the realizations of independent random variables following the same parametric distribution of the common parameter Θ_{12} . The evaluation of similarity between noisy patches can be then rephrased as the following hypothesis test:

$$\mathcal{H}_0 : \Theta_1 = \Theta_2 \equiv \Theta_{12} \quad (6)$$

$$\mathcal{H}_1 : \Theta_1 \neq \Theta_2. \quad (7)$$

A similarity criterion can be defined as a mapping from a pair of noisy patches $(\mathbf{x}_{1,j}, \mathbf{x}_{2,j})$ to a real value. According to the Neyman–Pearson theorem, the optimal criterion is the likelihood ratio test written as [29]

$$\Lambda^{(j)}(\mathbf{x}_{1,j}, \mathbf{x}_{2,j}) = \frac{p(\mathbf{x}_{1,j}, \mathbf{x}_{2,j}; \Theta_{12}, \mathcal{H}_0)}{p(\mathbf{x}_{1,j}, \mathbf{x}_{2,j}; \Theta_1, \Theta_2, \mathcal{H}_1)}. \quad (8)$$

Since the test $\Lambda^{(j)}(\mathbf{x}_{1,j}, \mathbf{x}_{2,j})$ is used to detect dissimilarity, the smaller the value for $\Lambda^{(j)}(\mathbf{x}_{1,j}, \mathbf{x}_{2,j})$, the more similar $\mathbf{x}_{1,j}$ and $\mathbf{x}_{2,j}$ are considered to be. Apart from the likelihood ratio test, other patch similarity criteria in the light of dissimilarity detection, such as Euclidean distance and Gaussian kernel and joint likelihood criteria and mutual information kernel, were reviewed in [29], and will not be introduced here.

B. TSLR Test

Using the patch similarity criteria $\Lambda^{(j)}(\mathbf{x}_{1,j}, \mathbf{x}_{2,j})$ defined in (8), we can evaluate if the two JS vectors $\mathbf{u}\mathbf{x}_1$ and $\mathbf{u}\mathbf{x}_2$ are statistically homogeneous. Here, a novel goodness-of-fit testing approach, which is referred to as the TSLR test statistic, is proposed to analyze the similarity between two JS vectors. Borrowing the idea of the two-sample KS test, we define the maximum patch dissimilarity as a measure of misfit for the TSLR test. Therefore, we have the following definition.

Definition 1: Let $\mathbf{u}\mathbf{x}_1$ and $\mathbf{u}\mathbf{x}_2$ be two time-series samples of mutually independent $k_1 \times k_2$ -dimensional random variables following the same parametric \mathcal{Z} distribution of common parameters Θ_{12} . Assuming $\mathbf{x}_{1,j}$ and $\mathbf{x}_{2,j}$ are two random variables from $\mathbf{u}\mathbf{x}_1$ and $\mathbf{u}\mathbf{x}_2$ in the SLC j , respectively, the hypothesis test for evaluating the patch similarity between $\mathbf{x}_{1,j}$ and $\mathbf{x}_{2,j}$ is shown in (6), and the parametric likelihood ratio is denoted in (8). The TSLR test statistic is defined as

$$D_T = \sup \left| -2 \log \Lambda^{(j)}(\mathbf{x}_{1,j}, \mathbf{x}_{2,j}) \right|, \quad j = 1, \dots, N. \quad (9)$$

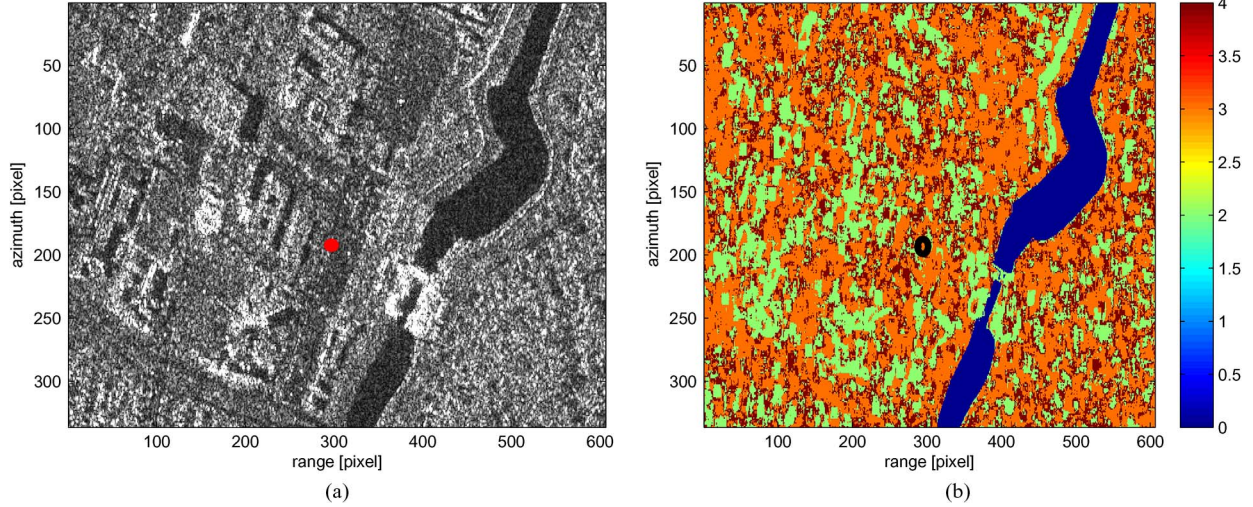


Fig. 2. Selection of best distribution using KS test. (a) SLC TerraSAR_X stripmap data over New Orleans. (b) Fitting results with $k_1 = k_2 = 9$, “1,” “2,” “3,” and “4” represent Rayleigh, lognormal, Weibull, and K distributions, respectively, and “0” denotes the region of noninterest. The red dot in (a) and black circle in (b) denote the pixel at (297, 192).

From Definition 1, we see that the TSLR test is based on a measure of the maximum log-likelihood ratio statistic and can be regarded as an extension of [29], which first proposed the use of a likelihood ratio test to define similarity. In practice, knowledge of parameters Θ_1 , Θ_2 , and Θ_{12} is unavailable. We usually replace them by their maximum-likelihood estimates (MLEs) so that the corresponding TSLR test based on the GLR $\Lambda_G^{(j)}$ is written as

$$D_T = \sup \left| -2 \log \Lambda_G^{(j)}(\mathbf{x}_{1,j}, \mathbf{x}_{2,j}) \right| \\ = \sup \left| -2 \log \left[\frac{p(\mathbf{x}_{1,j}; \hat{\Theta}_{12}) p(\mathbf{x}_{2,j}; \hat{\Theta}_{12})}{p(\mathbf{x}_{1,j}; \hat{\Theta}_1) p(\mathbf{x}_{2,j}; \hat{\Theta}_2)} \right] \right|. \quad (10)$$

It has been evaluated in [29] that the patch criterion based on $\Lambda_G^{(j)}$ is the most powerful since it is easy to implement and has good theoretical guarantees on the constant false-alarm rate and the uniformly most powerful invariance. In most situations, the exact distribution of D_T is not known. However, using a large sample theory, we can construct the asymptotic pdf for the TSLR test. More precisely, we have the following.

Theorem 1: Let ω_0 be a d -dimensional parameter space and $\Theta_1 \in \omega_0$, $\Theta_2 \in \omega_0$. Under the smoothness condition on the \mathcal{Z} distribution, as $k_1 \times k_2 \rightarrow \infty$, the pdf of the TSLR test statistic defined in (9) converges to

$$p_{D_T}(t; d) = N P_{\chi^2}(t; d)^{N-1} p_{\chi^2}(t; d) \quad (11)$$

where $P_{\chi^2}(t; d)$ and $p_{\chi^2}(t; d)$ are the cdf and the pdf of the chi-squared distribution with d degrees of freedom, respectively.

Proof: Under \mathcal{H}_0 and \mathcal{H}_1 in (6) and $\Theta_1 \in \omega_0$ and $\Theta_2 \in \omega_0$, we have

$$\mathcal{H}_0: \Theta_{12} \in \omega_0 \text{ versus } \mathcal{H}_1: (\Theta_1, \Theta_2) \in \Omega_0 - (\omega_0, \omega_0) \quad (12)$$

where ω_0 and Ω_0 have d and $2d$ free parameters, respectively. Using Wilks's theorem in [30], the (generalized) log-likelihood ratio statistic $-2 \log \Lambda^{(j)}$ has an approximate chi-squared distribution with d degrees of freedom, so that we have N i.i.d. chi-squared random variables: $-2 \log \Lambda^{(1)}$

$(\mathbf{x}_{1,1}, \mathbf{x}_{2,1}), \dots, -2 \log \Lambda^{(N)}(\mathbf{x}_{1,N}, \mathbf{x}_{2,N})$. The distribution of D_T is then written as

$$P(D_T \leq t) = P \left(-2 \log \Lambda^{(1)}(\mathbf{x}_{1,1}, \mathbf{x}_{2,1}) \leq t, \dots, \right. \\ \left. -2 \log \Lambda^{(N)}(\mathbf{x}_{1,N}, \mathbf{x}_{2,N}) \leq t \right) \\ = P_{\chi^2}(t; d)^N \quad (13)$$

and the corresponding pdf is given in Theorem 1.

Under Theorem 1, the null hypothesis that two JS vectors are homogeneous is rejected at a given significance level α if $D_T > C_\alpha$, where threshold C_α is found from $P(D_T \leq C_\alpha) = 1 - \alpha$ with $\alpha = 1 - P_{\chi^2}(t; d)^N$.

C. Similarity Analysis

Since the calculation of (generalized) log-likelihood ratios in the TSLR test depends on the types of distributions of SAR terrain clutter, it is necessary to determine which distribution fits the data best. There are various statistical distributions used to characterize the temporal and spatial amplitude distributions of SAR clutter, including Rayleigh, Weibull, lognormal, and K distribution. The classical Rayleigh distribution model for the amplitude of scatterers agrees reasonably well with observations of homogeneous regions with coarse spatial resolution [31]. Lognormal and Weibull distributions are good statistical representations of clutter in the case of a small-resolution cell or heterogeneous terrain, whereas the K distribution is highly suitable for modeling the terrain composed of a mixture of locally homogeneous patches [32]. We exploit a one-sample KS test to choose an appropriate distribution, i.e.,

$$D_{KS} = \sup |P_{k_1 \times k_2}(x) - P(x)| \quad (14)$$

where $P_{k_1 \times k_2}(x)$ is the cumulative amplitude distribution of scatterers in a SAR patch, and $P(x)$ is the pdf whose parameters can be obtained by the MLE technique. When the distribution that fits the data best is chosen, the TSLR test statistic D_T can be set up using the log-likelihood ratios developed in the Appendix.

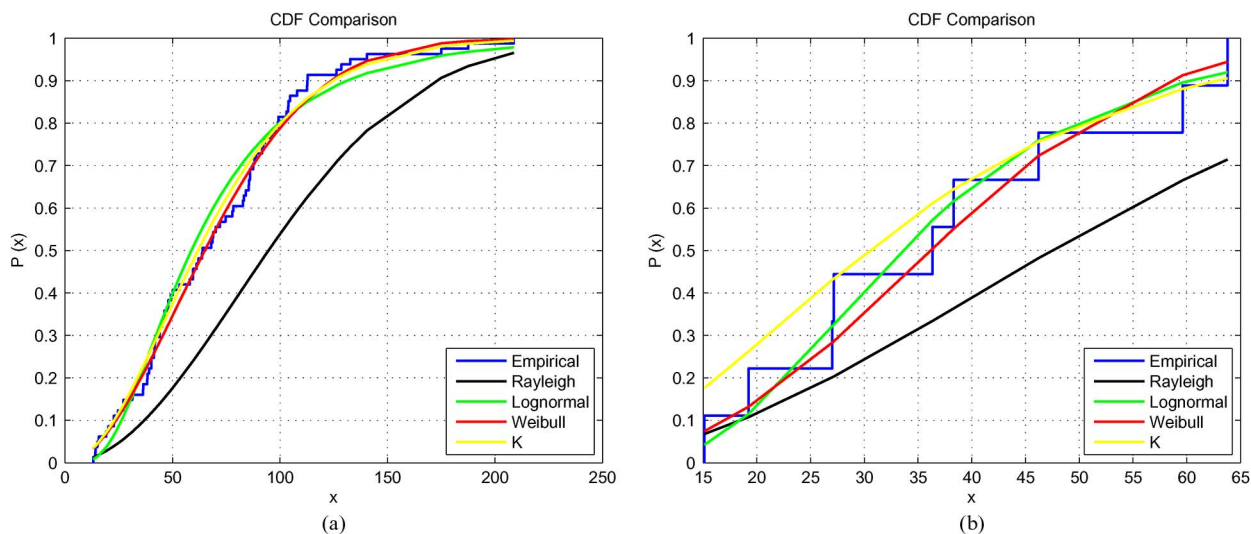


Fig. 3. CDF comparison for a pixel at (297, 192), “blue,” “black,” “green,” “red,” and “yellow” represent empirical, Rayleigh, lognormal, Weibull, and K cdfs, respectively. (a) $k_1 = k_2 = 9$. (b) $k_1 = k_2 = 3$.

An experiment on selecting the best distribution was conducted using a time series of TerraSAR-X SLC images over New Orleans. The size of the patch is set to $k_1 = k_2 = 9$. The empirical cdf was calculated and compared with theoretical Rayleigh, lognormal, Weibull, and K distributions whose pdfs are assumed time invariant. Fig. 3(a) shows the comparison result for a pixel located at the (297, 192) cell in the scene shown in Fig. 2(a). It is shown in Fig. 3(a) that the Rayleigh distribution fits the empirical measure worse than the last three distributions, which is probably due to a high spatial resolution in TerraSAR data. The values of the KS statistic for the last three distributions are 0.102, 0.059, and 0.081, respectively, indicating the Weibull distribution fits the scatterer best. Fig. 2(b) shows fitting results for the whole scene. Using a prior distribution in Fig. 2(b), the TSLR test can be carried out to choose homogeneous joint data vectors. It should be noted that the distribution fitting depends on the size of patch. Take the same pixel at (297, 192) for example. The fitting result is shown in Fig. 3(b), where the size of patch is set to $k_1 = k_2 = 3$. The corresponding values of the KS statistic are 0.303, 0.127, 0.158, and 0.209, respectively, indicating the lognormal distribution is the best choice for the pixel. Normally, the variation of types of distributions from pixel to pixel will be increased as the number of samples reduces. However, the difference of values of the KS statistic associated with the best and the second best distributions may be close, as shown in Fig. 3. Therefore, one can define the similar distributions whose statistic values are close when the size of patch is small. Given a certain search window, the procedure of similarity analysis includes two steps: 1) performing distribution fitting using the KS test from one of the SAR images and then selecting the patches that have the same distributions in the case of big size or that have similar distributions in the case of small size; and 2) carrying out the TSLR test for the selected patch stacks using the full data set. As shown in these two steps, the similarity analysis between two joint data vectors is a 2-D procedure since the first step is performed in the spatial dimension and the second step in the temporal dimension.

D. JS Filtering

Here, a new spatially adaptive filter, the JS filter, is proposed for JSInSAR. Spatially adaptive filtering aimed at reducing noise while preserving details is popularly used in speckle removal and interferogram filtering, as well as the covariance matrix estimation. Three key elements of spatially adaptive processing include: 1) the definition of a statistical test capable of choosing homogeneous pixels; 2) the calculation of weights assigned to the selected pixels; and 3) the determination of the searching area. Most existing spatially adaptive filters cannot be directly applied to the case of TSInSAR due to the lack of appropriate statistical tests for a stack of SAR data. In SqueeSAR, a spatially adaptive filter based on two-sample KS tests, which is referred to as DespecKS, was developed to process multitemporal SAR data sets. Different from DespecKS, the JS filtering exploits the TSLR test to select homogeneous patches and is not subject to the assumption of good coregistration. Moreover, we can introduce the weights to estimate the covariance matrix. The weight assigned to the homogeneous joint data vector $\mathbf{u}\mathbf{x}(l)$ is defined as

$$\xi(l) = e^{-\frac{D_T(l)}{C_\alpha}} \quad (15)$$

where $D_T(l)$ denotes the TSLR test applied to $\mathbf{u}\mathbf{x}(l)$ centered at the l th pixel. The form of $\xi(l)$ is similar to the weight of polarimetric SAR speckle filtering developed in [22]. The more similarity between two joint data vectors, the smaller $D_T(l)$ is and the bigger contribution $\mathbf{u}\mathbf{x}(l)$ have to the joint covariance matrix. With calculated weights, the joint covariance matrix $\mathbf{C}_{\mathbf{u}\mathbf{x}(m)}$ in (4) can be estimated by

$$\hat{\mathbf{C}}_{\mathbf{u}\mathbf{x}(m)} = \frac{1}{\sum_{l=1}^{|\Delta|} \xi(l)} \sum_{l \in \Delta} \xi(l) \mathbf{u}\mathbf{x}(l) \mathbf{u}\mathbf{x}^H(l) \quad (16)$$

where Δ is the set of homogeneous joint data vectors, and $\xi(l) = 1$ when $l = m$. The basic procedure of the JS filtering is described in Algorithm 1, and a corresponding illustration is provided in Fig. 4. The selection of the size of the patch (k_1, k_2) and the search window in Algorithm 1 can be

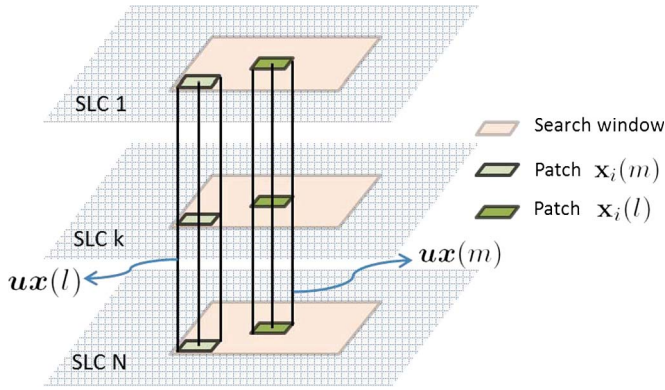


Fig. 4. JS filtering.

discussed using the Reed–Mallett–Brennan (RMB) rule [33]. Given k_1 , k_2 , and the number of SLCs N , the dimension of the joint covariance matrix is $k_1 \times k_2 \times N$. According to the RMB rule, the cardinality of the set Δ that $|\Delta| > 2(k_1 \times k_2 \times N) - 1$ would make the estimation loss within 3 dB. Therefore, one possible criterion is that the size of the search area is large enough to make sure that the number of homogeneous joint pixel vectors satisfies the RMB rule. Due to this criterion, the JS filtering is a nonlocal technique since the search area is not restricted to local neighboring pixels. The selected type of search area, which may be rectangular windows, directional windows, or spatially connected components, is subject to the topographic relief. For instance, one can select a rectangular window as the search window for locally flat terrains and a directional window for steep terrains. Given the size of the search window and N , the size and type of patches can be properly selected. For example, for small N , the patch may be set to 3×3 , whereas for large N , the patch can be constituted by three neighboring pixels in range and two neighboring pixels in azimuth. In addition, the selection of the size of the patch is related to the preservation of image details. It was investigated in [22] that, with the increase in size, textures and linear structures are better preserved, whereas the single-pixel point targets are blurred. To overcome the information loss of pointwise permanent scatterers, it is necessary to set threshold $C_{h_{jv}}$ for $|\Delta|$ prior to retrieval of the joint covariance matrix. It is difficult to define a universal criterion for the threshold $C_{h_{jv}}$ as it is dependent on the spatial resolution of the SAR data. However, since $C_{h_{jv}}$ is mainly used to preserve PSs, we can set this threshold according to the value of $|\Delta|$ for some typical permanent targets, such as buildings in the sites of interest. For example, if the average number of homogeneous joint data vectors for some pointwise targets is 30, we can set $C_{h_{jv}} = 30$.

Algorithm 1 JS Filtering of the TSLR Test

procedure:

- define a search window and the size of patch k_1, k_2 ;
- given a significance level α , calculate the test threshold C_α according to Theorem 1;
- set a certain threshold $C_{h_{jv}}$ for the number of homogeneous joint data vectors;
- **for** each joint data vector $\mathbf{u}\mathbf{x}(m)$ of image stacks **do**

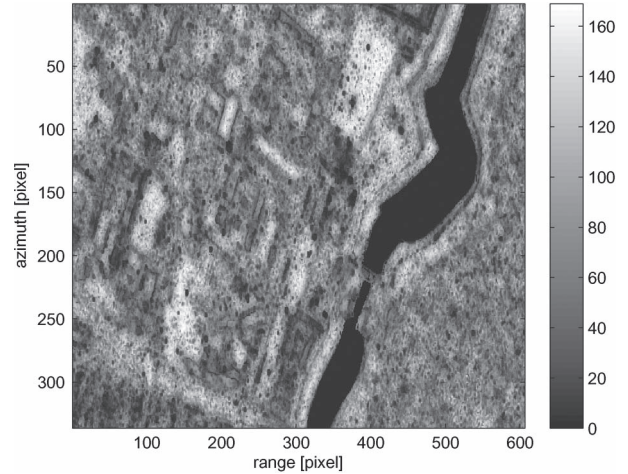


Fig. 5. Number of SHPs identified by the TSLR test.

- empty the set of homogeneous joint data vector Δ
- choose an appropriate distribution using (14)
- **for** each joint data vector $\mathbf{u}\mathbf{x}(l)$ in the search window as shown in Fig. 4 **do**
 - apply TSLR test to calculate D_T using (10).
 - **if** $D_T > C_\alpha$
 - discard the joint pixel stack $\mathbf{u}\mathbf{x}(l)$
 - **else**
 - add $\mathbf{u}\mathbf{x}(l)$ to Δ and compute the weight $\xi(l)$ using (15)
 - **end if**
- **end for**
- **if** $|\Delta| > C_{h_{jv}}$, estimate the covariance matrix $\hat{C}_{\mathbf{u}\mathbf{x}(m)}$ using (16)
- **end for**
- **end procedure**

To demonstrate the effectiveness of the proposed filter, 42 SLC TerraSAR-X Stripmap data over New Orleans are used. Since we are not interested in the canal at the site shown in Fig. 2(a), a mask is added for this experiment. The JS filter is compared with a 7×7 boxcar filter and a filter based on the KS test. For the JS filter, the search window is set to be 15×15 pixels, and the patch is a 3×3 window. Since the Rayleigh distribution is simple and has the similar fitting performance compared with more complex distributions when using a 3×3 patch, the distribution for the JS filter here is set to be Rayleigh. The number of statistically homogeneous patches (SHPs) identified by the TSLR test is shown in Fig. 5. In Fig. 5, one can see that the number of SHPs on the grass-covered sides of the levee near the canal is much higher than that on the concrete top of the levee, which indicates that some grass scatterers might become a PS. The original single-look image and its filtered versions using the boxcar filter, the filter based on the KS test, and the JS filter are shown in Figs. 2(a) and 6(a)–(c), respectively. Compared with the original image, although the speckle noise in Fig. 6(a) is reduced by using boxcar filtering, several details are missing due to blurring. Fig. 6(b) is the result using the filter based on the KS test with a 5×5 window, which shows good performance of edge and PS preserving; however, some details in the building area may be somewhat overly enhanced,

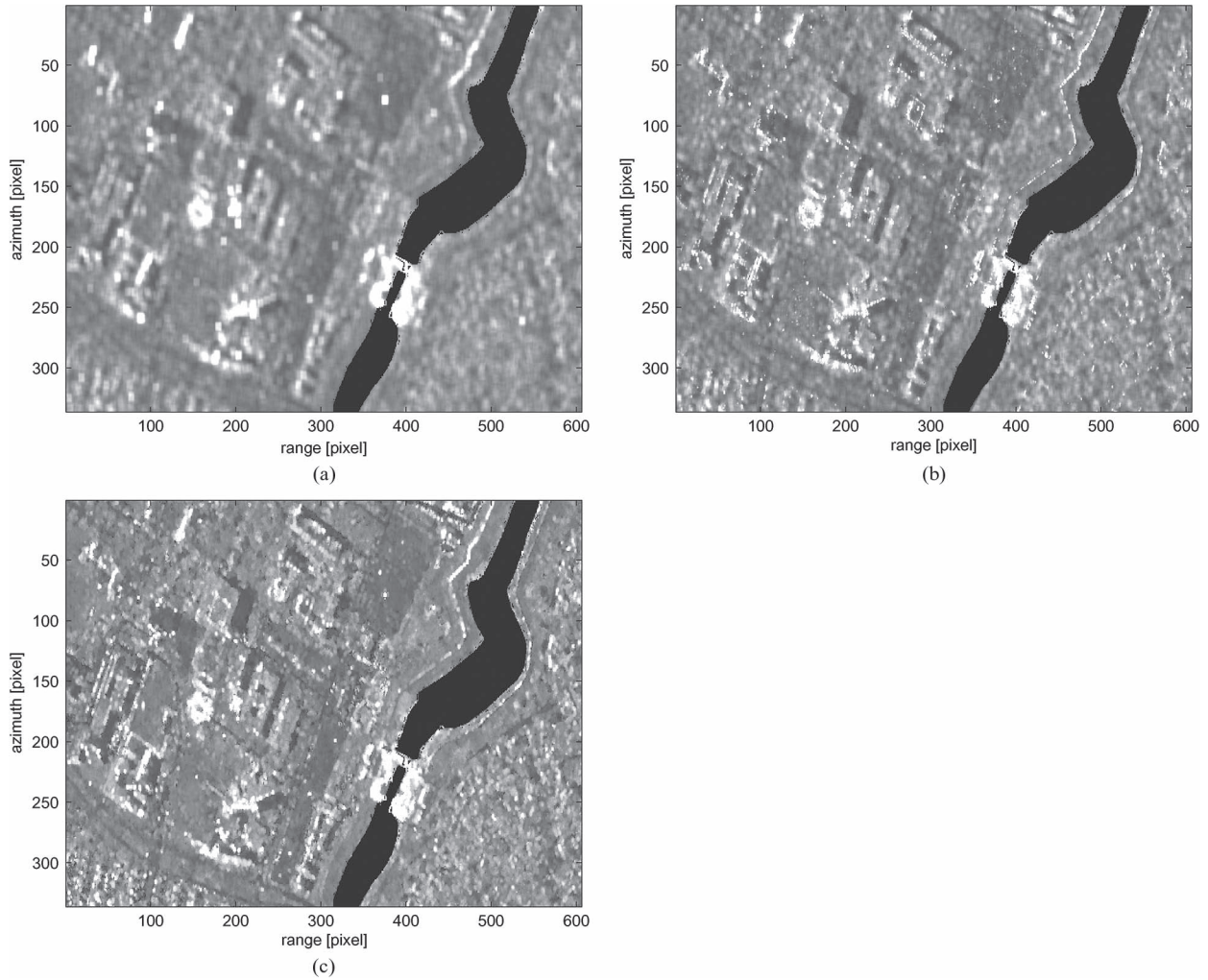


Fig. 6. Comparison of filtering algorithms using (a) 7×7 boxcar filter, (b) filter based on the KS test, and (c) JS filter.

and some details in statistically homogeneous areas, such as the grass-covered levees, may be somewhat noisy. This is because the single-pixel-based KS test does not make full use of similarity from neighboring pixels. Fig. 6(c) is the result using the proposed JS filter, where the details, including edges, linear, and curved features, and pointwise scatterers are well preserved, and the speckle is remarkably reduced. In Fig. 6(c), the grass-covered levee is more smooth than that in Fig. 6(b) since the patch-based TSLR test makes use of more details from local neighboring pixels. The comparisons in Fig. 6 indicate that the JS filter is applicable for statistically homogeneous areas.

IV. JSInSAR

A. Joint Subspace Projection

Prior to extracting geophysical parameters of interest using multiinterferogram-based techniques, a key stage of the second-generation TSInSAR is the estimation of the optimal wrapped interferometric phases from the estimated covariance matrix. The widely used methods to retrieve a set of phases are based on the MLE, including the phase linking algorithm in [34] and phase triangulation algorithm in [19]. The estimation technique exploited here is referred to as JSP, which was originally

proposed in [20] to retrieve the interferometric phase of an SLC pair. We extend JSP to the case of TSInSAR. The principle of JSP is based on projection of the joint signal subspace onto the corresponding joint noise subspace. Let us eigendecompose the estimated joint covariance matrix as

$$\hat{\mathbf{C}}_{\mathbf{u}\mathbf{x}(m)} = \mathbf{E}_s \mathbf{\Gamma}_s \mathbf{E}_s^H + \mathbf{E}_w \mathbf{\Gamma}_w \mathbf{E}_w^H \quad (17)$$

with

$$\begin{aligned} \mathbf{\Gamma}_s &= \text{diag} \left[\lambda^{(1)}, \lambda^{(2)}, \dots, \lambda^{(K)} \right] \\ \mathbf{\Gamma}_w &= \text{diag} \left[\lambda^{(K+1)}, \lambda^{(K+2)}, \dots, \lambda^{(k_1 \times k_2 \times N)} \right] \\ \mathbf{E}_s &= \left[\beta_{xuc}^{(1)}, \beta_{xuc}^{(2)}, \dots, \beta_{xuc}^{(K)} \right] \\ \mathbf{E}_w &= \left[\beta_{wuc}^{(K+1)}, \beta_{wuc}^{(K+2)}, \dots, \beta_{wuc}^{(k_1 \times k_2 \times N)} \right] \end{aligned}$$

where the eigenvalues in $\mathbf{\Gamma}_s$ and $\mathbf{\Gamma}_w$ are in descending order, and $\lambda^{(K)} \gg \lambda^{(K+1)}$. Eigenvectors $\beta_{wuc}^{(l)}$ ($l = K+1, \dots, k_1 \times k_2 \times N$) corresponding to the smaller eigenvalues $\lambda^{(l)}$ ($l = K+1, \dots, k_1 \times k_2 \times N$) span the joint noise subspace, i.e.,

$$\mathbf{N}_{uc} = \text{span} \left\{ \beta_{wuc}^{(K+1)}, \beta_{wuc}^{(K+2)}, \dots, \beta_{wuc}^{(k_1 \times k_2 \times N)} \right\} \quad (18)$$

whereas the larger eigenvectors $\beta_{xuc}^{(k)} (k = 1, 2, \dots, K)$ corresponding to the principle eigenvalues $\lambda^{(k)} (k = 1, 2, \dots, K)$ span the joint signal subspace, i.e.,

$$\mathbb{S}_{uc} = \text{span} \left\{ \beta_{xuc}^{(1)}, \beta_{xuc}^{(2)}, \dots, \beta_{xuc}^{(K)} \right\} \quad (19)$$

It is shown in (4) that $\hat{\mathbf{C}}_{\mathbf{u}x(m)}$ can be expressed as a function of the joint correlation function matrix $\hat{\mathbf{R}}_{\mathbf{u}x}$. By eigendecomposing $\hat{\mathbf{R}}_{\mathbf{u}x}$, an alternative form of $\hat{\mathbf{C}}_{\mathbf{u}x(m)}$ is written as

$$\begin{aligned} \hat{\mathbf{C}}_{\mathbf{u}x(m)} &= \mathbf{u}\mathbf{a}(\phi_m)\mathbf{u}\mathbf{a}^H(\phi_m) \odot \hat{\mathbf{R}}_{\mathbf{u}x} + \hat{\sigma}_{\mathbf{u}}\mathbf{w}^2\mathbf{I} \\ &= \mathbf{u}\mathbf{a}(\phi_m)\mathbf{u}\mathbf{a}^H(\phi_m) \odot \mathbf{E}_r\mathbf{\Gamma}_r\mathbf{E}_r^H + \hat{\sigma}_{\mathbf{u}}\mathbf{w}^2\mathbf{I} \end{aligned} \quad (20)$$

with

$$\begin{aligned} \mathbf{\Gamma}_r &= \text{diag} \left[\tilde{\lambda}^{(1)}, \tilde{\lambda}^{(2)}, \dots, \tilde{\lambda}^{(K)} \right] \\ \mathbf{E}_r &= \left[\beta_{xur}^{(1)}, \beta_{xur}^{(2)}, \dots, \beta_{xur}^{(K)} \right]. \end{aligned} \quad (21)$$

The noise power is often estimated by

$$\hat{\sigma}_{\mathbf{u}\mathbf{w}}^2 = \frac{1}{k_1 \times k_2 \times N - K} \sum_{l=K+1}^{k_1 \times k_2 \times N} \lambda^{(l)}. \quad (22)$$

As shown in (20), the same joint signal subspace based on the principle eigenvectors $\beta_{xuc}^{(k)} (k = 1, 2, \dots, K)$ of $\hat{\mathbf{C}}_{\mathbf{u}x(m)}$ can be spanned by the Hadamard product of $\mathbf{u}\mathbf{a}(\phi_m)$ and eigenvectors in \mathbf{E}_r , i.e.,

$$\begin{aligned} \mathbb{S}_{uc} &= \text{span} \left\{ \mathbf{u}\mathbf{a}(\phi_m) \odot \beta_{xur}^{(1)}, \mathbf{u}\mathbf{a}(\phi_m) \right. \\ &\quad \left. \odot \beta_{xur}^{(2)}, \dots, \mathbf{u}\mathbf{a}(\phi_m) \odot \beta_{xur}^{(K)} \right\} \end{aligned} \quad (23)$$

Due to the self-adjoint property of $\hat{\mathbf{C}}_{\mathbf{u}x(m)}$, the noise subspace spanned by eigenvectors in \mathbf{E}_w , as shown in (18), is orthogonal to the signal subspace shown in (23). Therefore, one can estimate the interferometric-phase vector ϕ_m by projecting the joint signal subspace onto the joint noise subspace, as follows:

$$\begin{aligned} J_c &= \sum_{k=1}^K \sum_{l=K+1}^{k_1 \times k_2 \times N} \left(\mathbf{u}\mathbf{a}(\phi_m) \odot \beta_{xur}^{(k)} \right)^H \\ &\quad \times \beta_{wuc}^{(l)} \beta_{wuc}^{(l)H} \left(\mathbf{u}\mathbf{a}(\phi_m) \odot \beta_{xur}^{(k)} \right) \end{aligned} \quad (24)$$

which is defined as the cost function to retrieve the optimal phase vector. Using in [20, Eq. (B.1)], we can rewrite the cost function of (24) as

$$J_c = \mathbf{u}\mathbf{a}^H(\phi_m) \left(\mathbf{E}_r\mathbf{E}_r^H \odot \mathbf{E}_w\mathbf{E}_w^H \right) \mathbf{u}\mathbf{a}(\phi_m). \quad (25)$$

To calculate the eigenvectors in \mathbf{E}_r for the cost function J_c , one can eigendecompose an estimate of the joint correlation function matrix that can be approximated as the absolute value of $(\hat{\mathbf{C}}_{\mathbf{u}x(m)} - \hat{\sigma}_{\mathbf{u}\mathbf{w}}^2\mathbf{I})$. It is noted that the computational complexity of minimization of J_c is too high due to the large dimension of the joint data vector. Under the assumption that

pixel stacks in the search window have an identical spatial steering vector, the cost function J_c can be simplified. Let

$$\mathbf{A} = \mathbf{E}_r\mathbf{E}_r^H \odot \mathbf{E}_w\mathbf{E}_w^H. \quad (26)$$

It can be easily proved that \mathbf{A} is a Hermitian matrix with the dimension $k_1 \times k_2 \times N$. Then

$$J'_c = \mathbf{a}^H(\phi_m) \left(\sum_{l_1=1}^{k_1 \times k_2} \sum_{l_2=1}^{k_1 \times k_2} \mathbf{A}_{l_1 l_2} \right) \mathbf{a}(\phi_m) \quad (27)$$

where $\mathbf{A}_{l_1 l_2}$ are $N \times N$ submatrices of $(\mathbf{E}_r\mathbf{E}_r^H \odot \mathbf{E}_w\mathbf{E}_w^H)$. It is indicated in (27) that, from a computational point of view, the main difference of our approach based on multidimensional testing and other TSInSAR based on 1-D testing lies in the calculation of the covariance matrix as the Hermitian matrix \mathbf{A} can be reduced to the sum of normal matrices prior to solving the minimization problem. Since the minimization of J'_c is an unconstrained quadratic optimization, one possible solution is to use a quasi-Newton method as in SqueeSAR, such as the Broyden–Fletcher–Goldfarb–Shanno method. Another option is to iteratively minimize J'_c with respect to each phase using the following closed form:

$$\hat{\vartheta}_n^{(q)} = \angle \left\{ \sum_{i \neq n}^N \left\{ \sum_{l_1=1}^{k_1 \times k_2} \sum_{l_2=1}^{k_1 \times k_2} \mathbf{A}_{l_1 l_2} \right\}_{i_p} \exp(j\hat{\vartheta}_i^{(q-1)}) \right\} \quad (28)$$

where q is the iteration step, and the operator $\angle\{\cdot\}$ indicates the phase of the element. The idea of an efficient algorithm using (28) comes from the phase linking algorithm in [34]. The starting point of iteration was assumed as the phase of the vector minimizing the quadratic form J'_c under the constraint $\mathbf{a}^{(0)}(\phi_m) = 1$. It is proven by the phase linking algorithm in [34] that such an iteration algorithm based on (28) is very effective when the joint covariance matrix is approximately known or accurately estimated.

Since some interferograms will have large temporal or spatial baselines, conventional InSAR coregistration methods may not be able to remove such high decorrelation. In StaMPS software from Delft [18], [35], a network method based on weighted least squares estimation was developed to perform the SAR scene coregistration in multiinterferogram time-series scenarios. However, if using JSP, one can still achieve the desired accuracy and the corresponding coherence even based on the conventional coregistration methods. In the following, we discuss the robustness of JSP with respect to coregistration errors. Suppose $N - 1$ SLCs are accurately coregistered and the last one has a coregistration error of one pixel. The pixel stacks in the joint data vector with a window of 3×3 shown in Fig. 1 is classified as the coherent pixel stacks ($[4-1, \dots, 4-k, \dots, 4-N]$, $[5-1, \dots, 5-k, \dots, 5-N]$, $[6-1, \dots, 6-k, \dots, 6-N]$, $[7-1, \dots, 7-k, \dots, 7-N]$, $[8-1, \dots, 8-k, \dots, 8-N]$, and $[9-1, \dots, 9-k, \dots, 9-N]$) and the noncoherent pixel stacks ($[1-1, \dots, 1-k, \dots, 1-N-1, 10-N]$, $[2-1, \dots, 2-k, \dots, 2-N-1, 11-N]$, and $[3-1, \dots, 3-k, \dots, 3-N-1, 12-N]$). The joint correlation function matrix $\mathbf{R}_{\mathbf{u}x}(5)$ can be decomposed into three terms, i.e.,

$$\mathbf{R}_{\mathbf{u}x}(5) = \mathbf{R}_1(5) + \mathbf{R}_2(5) + \mathbf{R}_3(5) \quad (29)$$

where

$$\mathbf{R}_1(5) = \begin{bmatrix} \mathbf{R}_x(4) & 0 & \cdots & 0 \\ 0 & \mathbf{R}_x(5) & \cdots & 0 \\ \vdots & \ddots & \cdots & 0 \\ 0 & \vdots & \mathbf{R}_x(9) & 0 \\ 0 & \vdots & \vdots & \ddots \\ 0 & \cdots & \cdots & 0 \end{bmatrix}$$

$$\mathbf{R}_2(5) = \begin{bmatrix} \ddots & & & \cdots & 0 \\ & \mathbf{R}_x(1) & & \cdots & 0 \\ 0 & 0 & & \cdots & 0 \\ 0 & \cdots & \mathbf{R}_x(2) & & 0 \\ 0 & 0 & & \cdots & 0 \\ 0 & \cdots & 0 & \mathbf{R}_x(3) & 0 \\ 0 & 0 & & \cdots & 0 \end{bmatrix}$$

$$\mathbf{R}_3(5) = \begin{bmatrix} \ddots & & \cdots & 0 \\ \vdots & \sigma_x^2(10) & \cdots & 0 \\ 0 & 0 & \ddots & 0 \\ 0 & \cdots & \sigma_x^2(11) & 0 \\ 0 & 0 & \ddots & 0 \\ 0 & \cdots & 0 & \sigma_x^2(12) \end{bmatrix}$$

are the joint correlation function matrices of the coherent pixel stacks, coherent pixel substacks, and noncoherent pixels, respectively. $\mathbf{R}_x(4), \dots, \mathbf{R}_x(9)$ in $\mathbf{R}_1(5)$ are $N \times N$ correlation matrices; $\mathbf{R}_x(1), \mathbf{R}_x(2)$, and $\mathbf{R}_x(3)$ in $\mathbf{R}_2(5)$ are $(N-1) \times (N-1)$ correlation matrices; and $\sigma_x^2(10), \sigma_x^2(11)$, and $\sigma_x^2(12)$ in $\mathbf{R}_3(5)$ are echo powers of the pixels. Using (29), $\mathbf{C}_{\mathbf{u}\mathbf{x}(5)}$ can be eigendecomposed into

$$\begin{aligned} \mathbf{C}_{\mathbf{u}\mathbf{x}(5)} &= \mathbf{u}\mathbf{a}(\phi_5)\mathbf{u}\mathbf{a}^H(\phi_5) \odot (\mathbf{R}_1(5) + \mathbf{R}_2(5) + \mathbf{R}_3(5)) \\ &\quad + \sigma_{\mathbf{u}\mathbf{w}}^2 \mathbf{I} \\ &= \mathbf{u}\mathbf{a}(\phi_5)\mathbf{u}\mathbf{a}^H(\phi_5) \odot (\mathbf{R}_1(5) + \mathbf{R}_2(5)) + \mathbf{R}_3(5) \\ &\quad + \sigma_{\mathbf{u}\mathbf{w}}^2 \mathbf{I} \\ &= \mathbf{u}\mathbf{a}(\phi_5)\mathbf{u}\mathbf{a}^H(\phi_5) \odot \mathbf{E}_{r1}\mathbf{\Gamma}_{r1}\mathbf{E}_{r1}^H + \mathbf{E}_{r2}\mathbf{\Gamma}_{r2}\mathbf{E}_{r2}^H \\ &\quad + \mathbf{E}_w\mathbf{\Gamma}_w\mathbf{E}_w^H \end{aligned} \quad (30)$$

where

$$\begin{aligned} \mathbf{\Gamma}_{r1} &= \text{diag} [\tilde{\lambda}^{(1)} + \sigma_{\mathbf{u}\mathbf{w}}^2, \tilde{\lambda}^{(2)} + \sigma_{\mathbf{u}\mathbf{w}}^2, \dots, \tilde{\lambda}^{(9)} + \sigma_{\mathbf{u}\mathbf{w}}^2] \\ \mathbf{E}_{r1} &= [\beta_{xur}^{(1)}, \beta_{xur}^{(2)}, \dots, \beta_{xur}^{(9)}] \\ \mathbf{\Gamma}_{r2} &= \text{diag} [\tilde{\lambda}^{(10)} + \sigma_{\mathbf{u}\mathbf{w}}^2, \tilde{\lambda}^{(11)} + \sigma_{\mathbf{u}\mathbf{w}}^2, \tilde{\lambda}^{(12)} + \sigma_{\mathbf{u}\mathbf{w}}^2] \\ \mathbf{E}_{r2} &= [\beta_{xur}^{(10)}, \beta_{xur}^{(11)}, \beta_{xur}^{(12)}] \\ \mathbf{\Gamma}_w &= \text{diag} [\sigma_{\mathbf{u}\mathbf{w}}^2, \dots, \sigma_{\mathbf{u}\mathbf{w}}^2], \\ \mathbf{E}_w &= [\beta_{wuc}^{(1)}, \beta_{wuc}^{(2)}, \dots, \beta_{wuc}^{(9N-12)}]. \end{aligned} \quad (31)$$

It is shown in (30) that $\mathbf{u}\mathbf{a}(\phi_5) \odot \beta_{xur}^{(k)}$ ($k = 1, 2, \dots, 9$) and $\beta_{xur}^{(k)}$ ($k = 10, 11, 12$) span the joint signal subspace, and $\beta_{wuc}^{(l)}$ ($l = 13, \dots, 9N-12$) span the joint noise subspace. The dimension of the joint signal subspace is equal to 12, which is increased by 3 in comparison with that in the case of accurate coregistration due to the introduction of three noncoherent pixels in $\mathbf{R}_3(5)$. The projection of the joint signal subspace onto the corresponding joint noise subspace is written as

$$\begin{aligned} \min\{J_c\} &= \min\{\mathbf{u}\mathbf{a}^H(\phi_5)(\mathbf{E}_{r1}\mathbf{E}_{r1}^H \odot \mathbf{E}_w\mathbf{E}_w^H)\mathbf{u}\mathbf{a}(\phi_5) \\ &\quad + (\mathbf{E}_{r2}\mathbf{E}_{r2}^H \odot \mathbf{E}_w\mathbf{E}_w^H)\} \\ &= \min\{\mathbf{u}\mathbf{a}^H(\phi_5)(\mathbf{E}_{r1}\mathbf{E}_{r1}^H \odot \mathbf{E}_w\mathbf{E}_w^H)\mathbf{u}\mathbf{a}(\phi_5)\}. \end{aligned} \quad (32)$$

As noted from (32), the joint correlation function matrix $\mathbf{R}_3(5)$ of the noncoherent pixels has no contribution to retrieval of the phase vector ϕ_5 . Since the noncoherent pixels in the joint data vector have no effect on the estimation of ϕ_5 , it indicates that our technique is robust with respect to coregistration errors.

B. Procedure of JSInSAR

In the framework of SqueeSAR, two procedures including preprocessing and PSI are integrated to extract geophysical parameters from both DSs and PSs. The benefit of such framework is that it efficiently avoids the hybrid processing chain where two or more algorithms may be applied to DSs and PSs separately, which motivates us to exploit a similar processing chain. The preprocessing in JSInSAR includes the JS filtering and JSP. The procedure of JSInSAR is described as follows.

- Step 1) Define the sizes of the search window and the patch for each desired pixel m and set thresholds $C_\alpha, C_{h_{jv}}$, and the type of distribution used in the JS filter.
- Step 2) Construct the joint data vector for each m and apply the JS filter to estimate the joint covariance matrix $\hat{\mathbf{C}}_{\mathbf{u}\mathbf{x}(m)}$.
- Step 3) Estimate joint signal and noise subspaces by eigendecomposing the joint covariance matrix and joint correlation function matrix.
- Step 4) Retrieve an optimal phase vector for the desired pixel stack m by projecting the joint signal subspace onto the joint noise subspace.
- Step 5) Choose pixels whose temporal coherence is higher than a certain threshold and substitute the original phase values with their optimized ones.
- Step 6) Process the updated SAR images using PSI technique and retrieve geophysical parameters including elevation and time-series displacement.

Since the PSI technique is used in the last step, the performance assessment of JSInSAR such as the standard deviation (std) of displacement measurements is similar with that in PSI. The relation between the SNR of PSs or equivalent PSs converted from DSs and the variance of displacement rate can be expressed as [36]

$$\sigma_v^2 \approx \frac{-2\lambda^2 \ln \frac{\text{SNR}}{1+\text{SNR}}}{N(4\pi\sigma_T)^2} \quad (33)$$

where the temporal baseline dispersion σ_T^2 is given by $\sum_{i=1}^N (T_i - \bar{T})^2 / N$. The difference of σ_v^2 in PSI and JSInSAR is the calculation of SNR for PSs and the equivalent PSs. Compared with the SNR of PSs, the SNR of equivalent PSs is not only related to the size of scatterer and the sampling cell but also related to the parameters of the JS filter such as the number of neighboring pixels. As the number of neighboring pixels increases, the phase noise is reduced, but the error of spatial correlation may be included since an error in one pixel is highly correlated with errors at its similar neighbors. It is difficult to derive a calculating formula of the SNR for the equivalent PSs with respect to the number of neighboring pixels since we do not exactly know how the phase noise changes with the size of a patch and how the process of combining information from neighboring pixels affects the spatial correlation of errors. Therefore, we still use the original temporal coherence defined in PSI to extract the variance of displacement measurement, i.e., [36]

$$\sigma_v^2 \approx \frac{-2\lambda^2 \ln \gamma}{N(4\pi\sigma_T)^2} \quad (34)$$

where γ is the temporal coherence of equivalent PSs in the updated SAR image. Although we do not know how the spatial correlation of errors change with the size of a patch, one can use the following extended temporal coherence as defined in [19] to assess the quality of the estimated phase vector and the effect of spatial correlation from neighboring pixels

$$\gamma_{\text{jsp}} = \frac{2}{N^2 - N} \text{Re} \sum_{n=1}^N \sum_{k=n+1}^N \exp(j\varphi_{nk}) \exp(-j(\vartheta_n - \vartheta_k)). \quad (35)$$

C. Computational Complexity Analysis

The processing time of the proposed JSInSAR depends on three parts: joint scattering filtering, JSP, and PSI technique. In order to compare with other existing TSInSAR, such as, PSI and SqueeSAR, we only need to analyze the computational burden of the preprocessing (i.e., the first two parts). For a given SAR image with height M_1 and width M_2 and a $W_1 \times W_2$ search window, assuming the calculation complexity of the TSLR test, the joint covariance matrix and JSP are T_{jt} , T_{jc} , and T_{jsp} , respectively, and the total time of the preprocess of JSInSAR is around $M_1 \times M_2 \times [W_1 \times W_2 \times (T_{jt} + T_{jc}) + T_{jsp}]$. Similarly, the computational burden of the individual-pixel-based preprocess as in SqueeSAR is $M_1 \times M_2 \times [W_1 \times W_2 \times (T_{ot} + T_{oc}) + T_{phe}]$, where T_{ot} , T_{oc} , and T_{phe} denote the calculation time of the 1-D test, the covariance matrix, and the phase estimation. It is indicated in (27) that, from a computational point of view, the main difference of JSP and other phase estimation algorithms lies in the calculation of the covariance matrix. In other words, if the joint covariance matrix is decomposed into submatrices, T_{jsp} is close to T_{phe} and $T_{jc} \approx k_1 \times k_2 \times T_{oc}$, where k_1 and k_2 are the size of the patch. The main difference between T_{jt} and T_{ot} is the time used in the MLE of the parameters, as shown in the Appendix, which

TABLE I
TERRASAR-X ACQUISITION DATES, TIME INTERVALS,
AND PERPENDICULAR BASELINES

No.	Date	Interval[days]	Baseline[m]	No.	Date	Interval[days]	Baseline[m]
1	2009-03-13	-495	-145.53	22	2011-09-12	418	-89.00
2	2009-04-15	-462	-25.30	23	2011-10-15	451	92.82
3	2009-05-18	-429	-77.32	24	2011-10-26	462	1.55
4	2009-06-20	-396	-130.56	25	2011-11-17	484	-103.33
5	2009-07-23	-363	-6.37	26	2011-11-28	495	-152.72
6	2009-08-25	-330	-118.65	27	2011-12-09	506	-252.21
7	2009-09-27	-297	-27.86	28	2011-12-20	517	-13.85
8	2009-10-30	-264	-131.07	29	2012-01-11	539	-173.40
9	2009-12-02	-231	-168.35	30	2012-01-22	550	5.97
10	2010-01-15	-187	-114.47	31	2012-02-13	572	-45.88
11	2010-02-06	-165	2.63	32	2012-02-24	583	-39.07
12	2010-03-11	-132	4.11	33	2012-03-17	605	-4.58
13	2010-04-13	-99	-157.02	34	2012-03-28	616	-42.40
14	2010-05-16	-66	-130.01	35	2012-04-30	649	71.52
15	2010-06-18	-33	-81.77	36	2012-05-11	660	66.84
16	2010-07-21	0	0	37	2012-06-24	704	-216.60
17	2010-08-23	33	-211.59	38	2012-07-05	726	-83.90
18	2010-10-28	99	-90.29	39	2012-07-16	748	-41.53
19	2011-06-16	330	-150.74	40	2012-07-27	737	138.24
20	2011-07-19	363	45.19	41	2012-08-07	748	-68.27
21	2011-08-10	385	-153.90	42	2012-08-18	759	-225.66

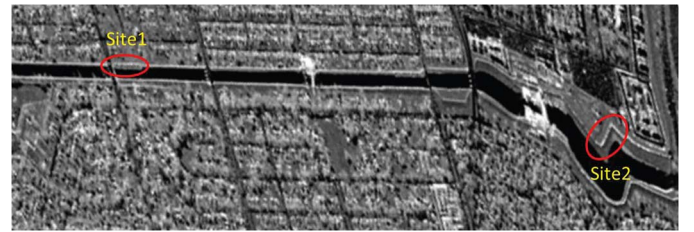


Fig. 7. Reflectivity image of the region of interest.

is proportional to the number of scatterers in each SAR patch, i.e., $k_1 \times k_2$. Therefore, the calculation complexity of preprocessing in JSInSAR is approximately $k_1 \times k_2$ times larger than that preprocessing. In order to mitigate the processing time, a mask for the region of interest is usually used to perform the preprocess for JSInSAR.

V. EXPERIMENTAL RESULTS AND ANALYSIS

Forty-two TerraSAR-X Stripmap images over New Orleans were acquired between March 2009 and August 2012 in the descending orbit. TerraSAR works in X-band (9.6-GHz frequency) and acquires high-quality high-resolution (1 m) SAR images. The data set used is presented in Table I. All were resampled and coregistered to the same master acquisition, 2010-07-21. Here, we selected two sections of the grass-covered levee located at London Ave Canal as the experimental scenes shown in Fig. 7.

In the experiment, the search window is set to be 21×23 pixels, and the size of the patch is 3×3 . A mask for the grass-covered levee area is used to perform the preprocessing in JSInSAR. The threshold for homogeneous joint data vectors is set to be 5. Figs. 8 and 9 show the displacement-rate maps of Site 1 using standard PSI and the proposed JSInSAR. The number of measurement points identify by PSI is 35, whereas the best DSs every 21×23 pixels to have independent measurement points equivalent to PSs are 82

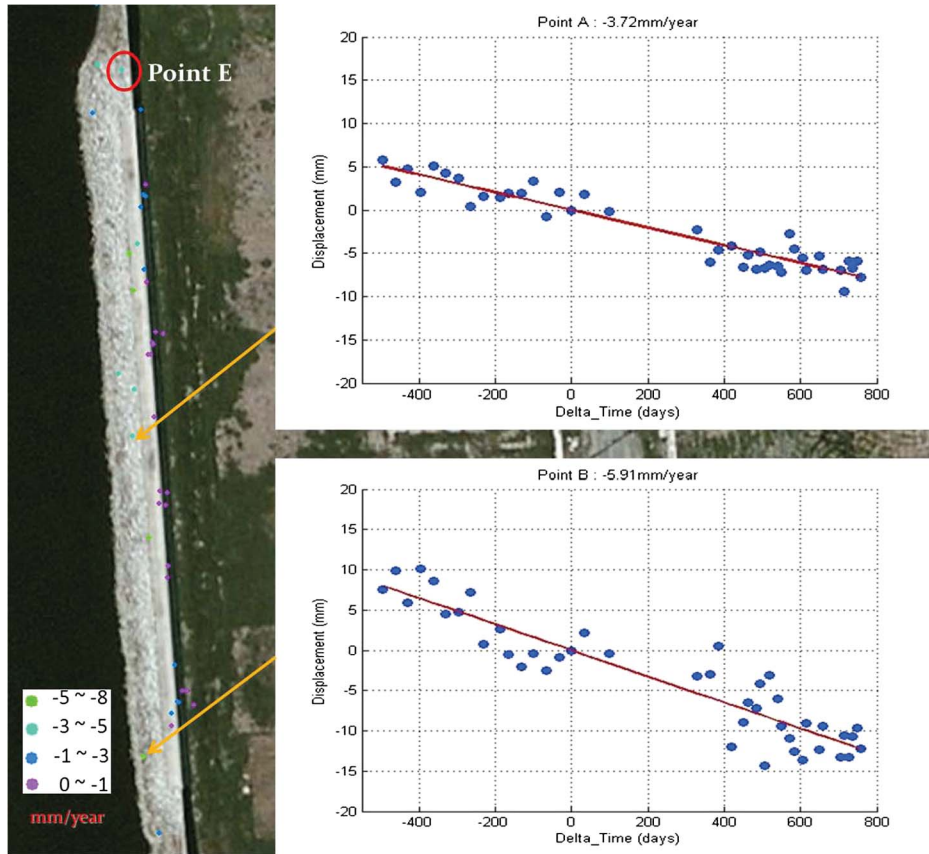


Fig. 8. Displacement-rate image of Site 1 overlaid on Google map using PSI. A negative rate denotes subsidence along LOS. The size of each identified target is 1 m.

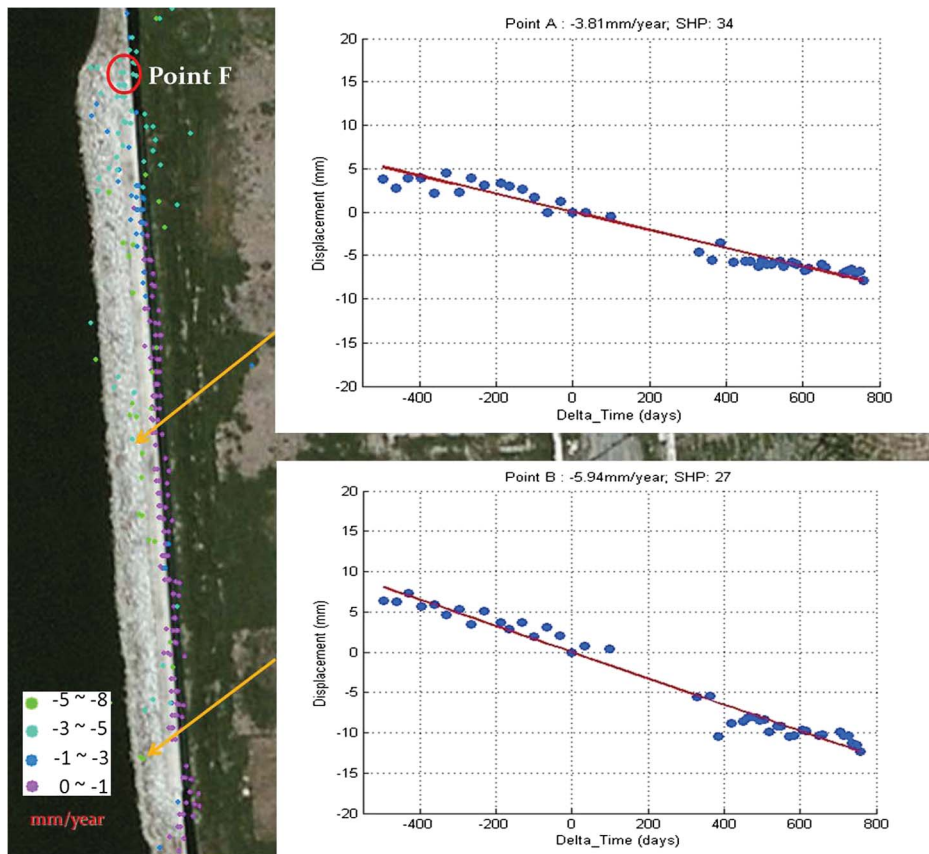


Fig. 9. Displacement-rate image of Site 1 overlaid on Google map using JSInSAR. A negative rate denotes subsidence along LOS. The size of each identified target is 1 m.

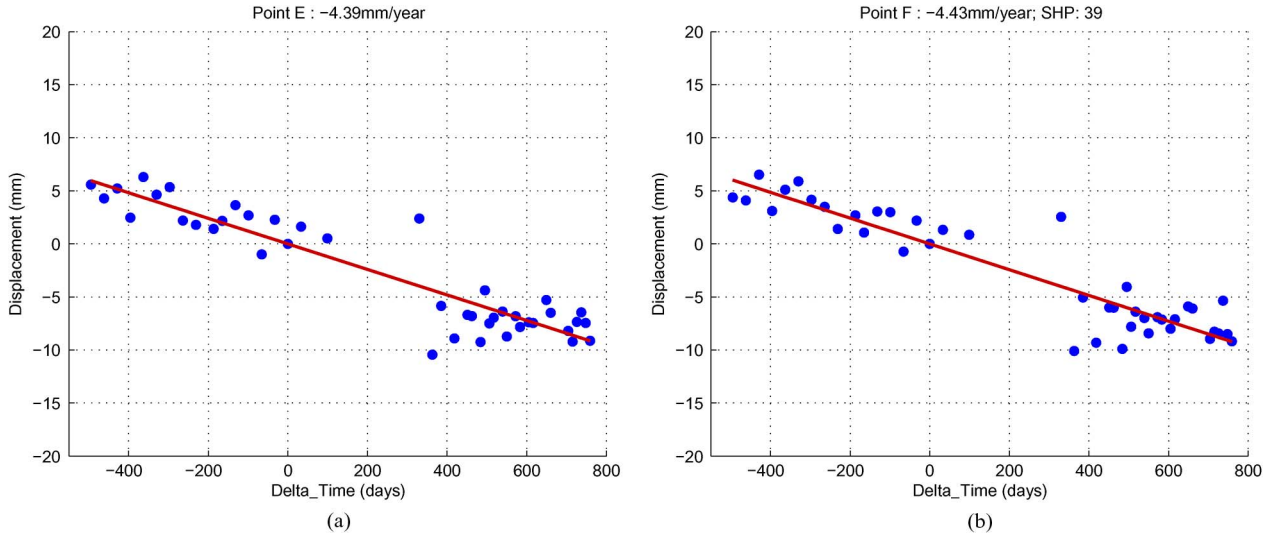


Fig. 10. Displacement time series for (a) Point E in Fig. 8 and (b) Point F in Fig. 9.



Fig. 11. Displacement-rate image of Site 2 overlaid on Google map using PSI. A negative rate denotes subsidence along LOS. The size of each identified target is 1 m.



Fig. 12. Displacement-rate image of Site 2 overlaid on Google map using JSInSAR. A negative rate denotes subsidence along LOS. The size of each identified target is 1 m.

when using JSInSAR. This indicates that the spatial density of measurement points is significantly increased by using JSInSAR in comparison with PSI since the SNR of a part of the DS is enhanced enough to exceed a certain coherence threshold (0.85) using JS processing. The time series of displacement for Points A and B by applying PSI and JSInSAR are shown in the inserted pictures of Figs. 8 and 9, respectively. The standard deviation of displacement of Points A and B are reduced from 1.4 to 0.92 and from 2.83 to 1.21 by using JSInSAR. Therefore, the quality of the displacement time series can be improved using the proposed technique. For better validation, the time series for newly detected DS (Point F) with the red circle in Fig. 9 and the surrounding detected PS (Point E) with the red circle in Fig. 8 are shown in Fig. 10(a) and (b), respectively, where the time series are almost consistent. This can be a good indication of the feasibility of the proposed algorithm.

The displacement-rate map of Site 2 using PSI is shown in Fig. 11, where one can see that plenty of measurement points are detected on the concrete top of the levee, whereas no points

can be found on the two sides of the levee due to low reflectivity and the low SNR of grass. By applying JS processing, one can observe from Fig. 12 that a good number of measurement points on the grass-covered sides are found due to the fact that the numbers of patches centered at these points sharing the same statistical behavior are large enough to make their coherence exceed the threshold. The displacement time series for Points C and D in Fig. 12 are shown in Fig. 13(a) and (b), respectively. The numbers of SHPs for Points C and D are 238 and 87, respectively. Comparing Fig. 13(a) with Fig. 13(b), one can see that the standard deviation of the time-series displacement in Fig. 13(a) is lower than that in Fig. 13(b) since the number of SHPs for Point C is larger than that for Point D. A scatter plot showing the RMS residual to the linear velocity fit versus the number of SHP for all the JSs in Site 2 is shown in Fig. 14, where we can see that the RMS residual generally declines as the number of SHP increases. This indicates that combining information from SHPs helps improve the SNR and makes the results comparable to PS.

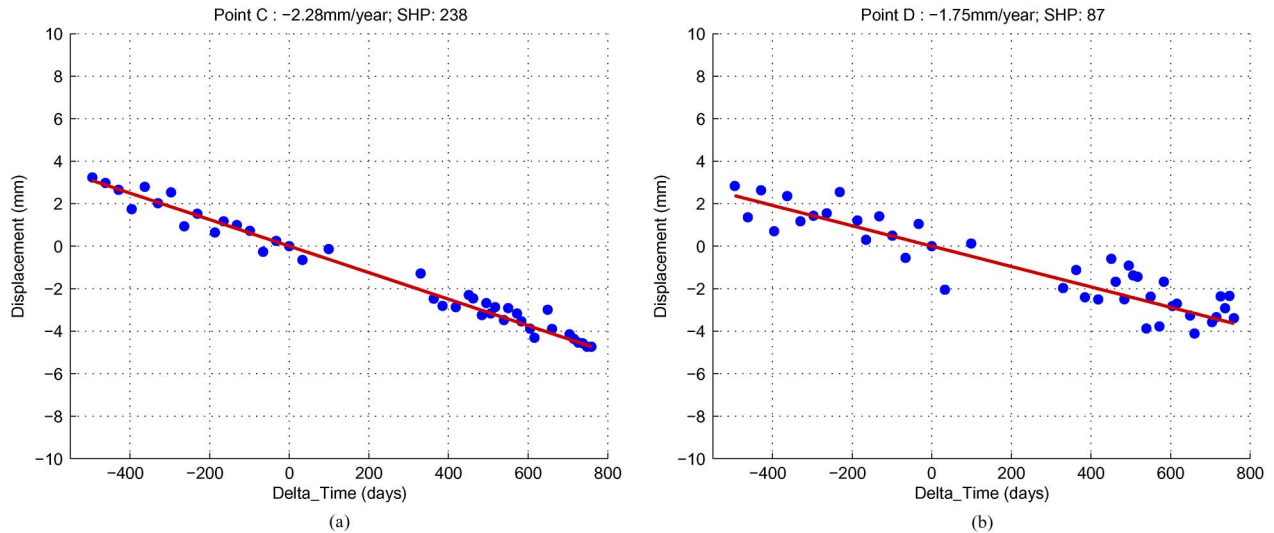


Fig. 13. Displacement time series using JSInSAR for (a) Point C and (b) Point D.

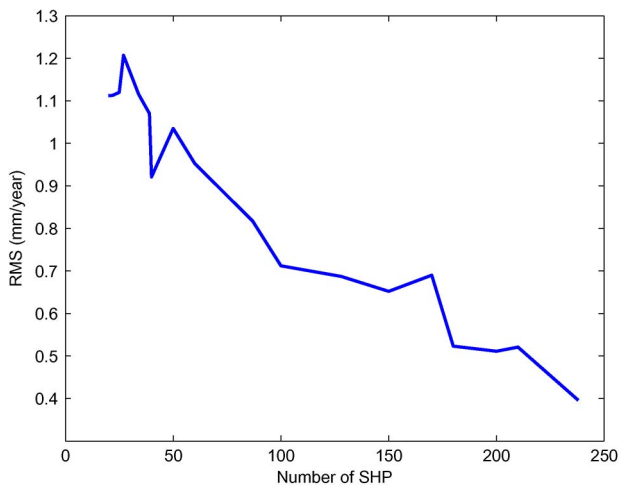


Fig. 14. RMS residual varied with the number of SHP for all JSs in Site 2.

Although the density of measurement points is increased by using JSInSAR as shown from the results in both Sites 1 and 2, the estimated time-series results have variable spatial resolution since a different number of SHPs are used for each desired pixel. This is allowed in some cases such as homogeneous grass-covered areas with small topographic relief. However, it may cause the information loss, for example, the sharp variation of deformation across faults in urban areas. To mitigate this effect, directional windows for the selection of the patch and search area in JS filtering are recommended to be used for the terrains with sharp variation of height or deformation.

Next, another experiment was conducted to verify the robustness of JSInSAR with respect to coregistration errors. A few SLCs (2, 6, 8, 10, 11, 14, 19, 21, 23, 25, 27, 31, 32, 35, 37, 38, 39, 41 shown in Table I) are randomly selected and have one-pixel coregistration errors with respect to the reference SLC, and the remainder of SLCs are accurately coregistered. Fig. 15(a) and (b) shows the interferograms in the case of the accurate coregistration, and Fig. 15(c) and (d) show the

interferograms in the case of the one-pixel coregistration error. Interferograms in Fig. 15(a), (c) and (b), (d) are obtained by the conventional processing (i.e., direct subtraction of the slave phase from the master phase) and JSP, respectively. Comparing Fig. 15(a) and (b), one can observe that the phase noise is suppressed significantly by JSP. When the coregistration error reaches one pixel, the corresponding pixel pair is completely decorrelated so that no interferometric fringes can be found in Fig. 15(c). However, by using the proposed technique, one can still find clear interferometric fringes in Fig. 15(d), which indicates that our technique does not suffer from the large coregistration error. Fig. 16 shows temporal coherence calculated using (35) for JSInSAR in the case of fine coregistration and a one-pixel coregistration error. Comparing Fig. 16(a) with (b), one can observe that the large coregistration error has little effect on the temporal coherence. The average temporal coherence in Fig. 16(a) and (b) are 0.64 and 0.61, respectively, indicating that the proposed technique is robust even in the case of a large coregistration error.

VI. CONCLUSION

In the paper, a new second-generation TSInSAR referred to as JSInSAR is proposed by taking advantage of the coherence information of neighboring pixel stacks. The key concepts, including the TSLR test statistic, JS filtering, and extended JSP, are developed and integrated in JSInSAR. In addition to the increase in the spatial density of measurement points and the quality improvement of the displacement time series, JSInSAR is also able to provide reliable geophysical parameters in the presence of large coregistration errors. However, as noted in the procedure of the TSLR test, a prior distribution of SAR clutter needs to be determined. In other words, the proposed JS filter of TSLR testing is not distribution free. This will reduce the computational efficiency. Furthermore, more GLRs need to be developed for those distributions that are not included in the Appendix.

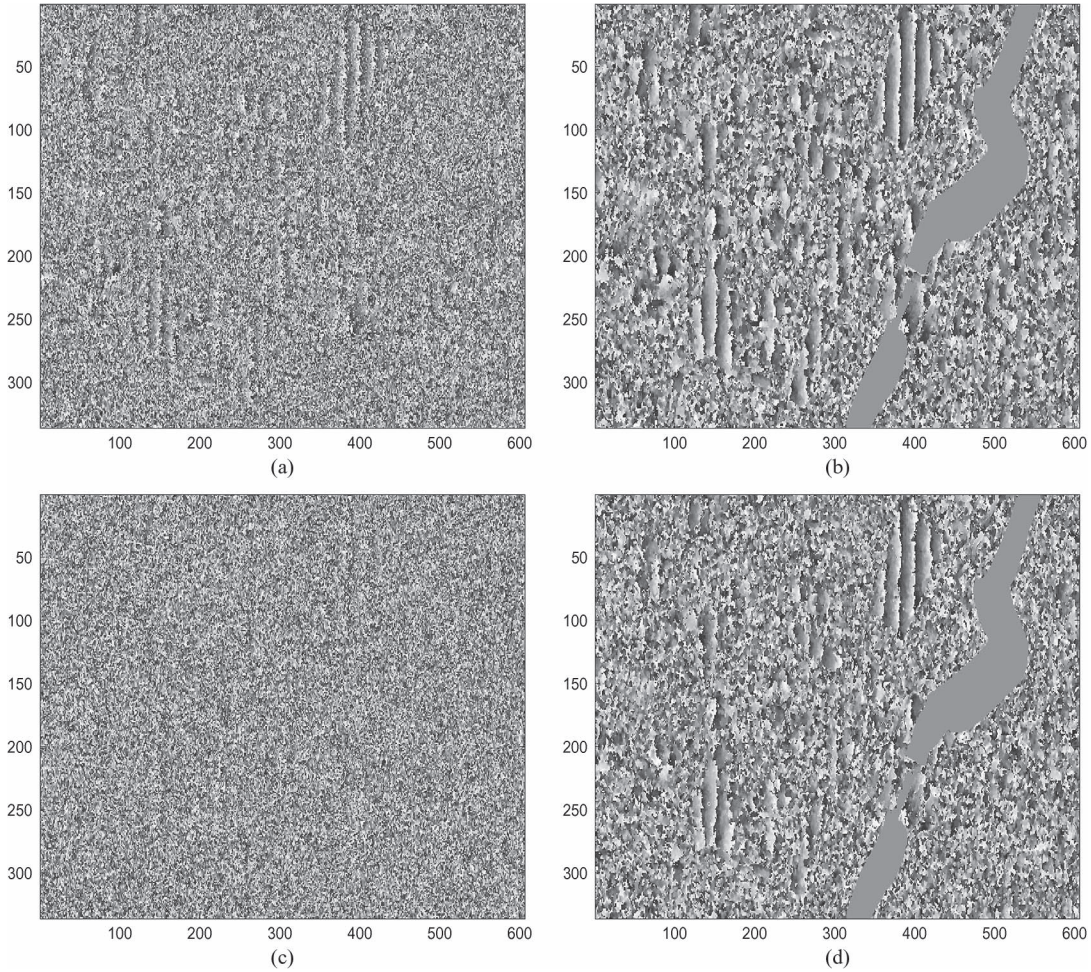


Fig. 15. Interferograms obtained by (a) conventional processing and (b) the proposed technique for the accurate coregistration in comparison with those obtained by (c) conventional processing and (d) the proposed technique for coregistration error up to one pixel.

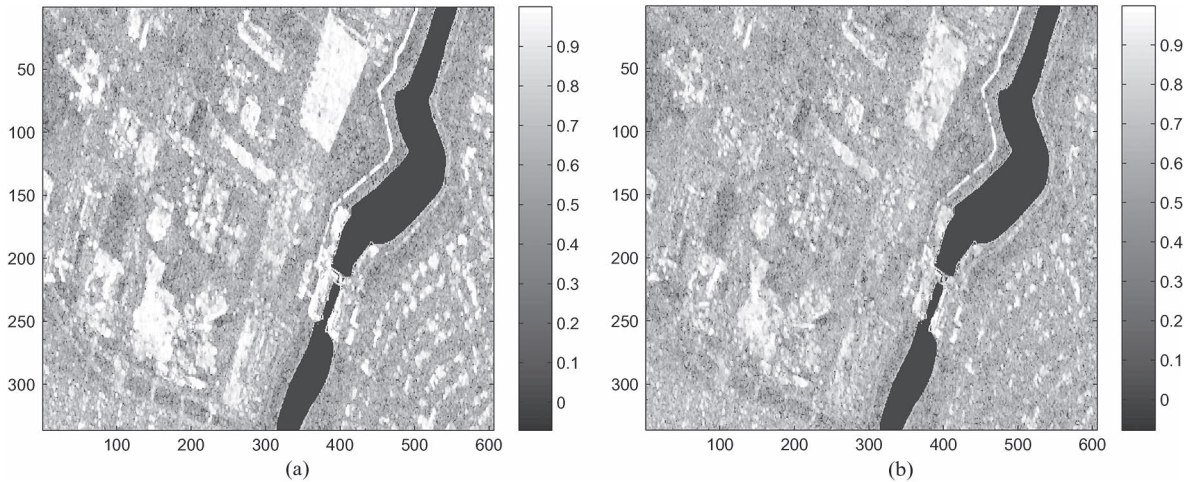


Fig. 16. Temporal coherence comparison between (a) accurate coregistration and (b) coregistration error up to one pixel.

APPENDIX

GLRS FOR SAR PATCH SIMILARITY USING RAYLEIGH, LOGNORMAL, WEIBULL, AND THE K DISTRIBUTIONS

A) *Rayleigh Distribution:* Let k_0 be the number of scatterers in each SAR patch. Under the Gaussian scattering assumption [25], the amplitudes of scatterers in two SAR patches \mathbf{x}_1 and \mathbf{x}_2 follow Rayleigh distribution with parameter η , i.e., $x_{1i} \sim$

$p_R(x; \eta_1)$ and $x_{2i} \sim p_R(x; \eta_2)$, $i = 1, \dots, k_0$. The hypothesis test for patch similarity can be described as $\mathcal{H}_0 : \eta_1^2 = \eta_2^2 = \eta^2$ against $\mathcal{H}_1 : \eta_1^2 \neq \eta_2^2$. The GLR under Rayleigh distribution is given by [37]

$$\Lambda_R(\mathbf{x}_1, \mathbf{x}_2) = \frac{(\hat{\eta}_1^2)^{k_0} (\hat{\eta}_2^2)^{k_0}}{(\hat{\eta}^2)^{2k_0}} \tag{36}$$

where $\hat{\eta}_1^2$, $\hat{\eta}_2^2$, and $\hat{\eta}^2$ are the MLEs and written as

$$\hat{\eta}_1^2 = \frac{1}{k_0} \sum_{i=1}^{k_0} x_{1i}^2 \quad \hat{\eta}_2^2 = \frac{1}{k_0} \sum_{i=1}^{k_0} x_{2i}^2 \quad \hat{\eta}^2 = \frac{\hat{\eta}_1^2 + \hat{\eta}_2^2}{2}. \quad (37)$$

B) Lognormal Distribution: We assume that the amplitudes of scatterers in two SAR patches \mathbf{x}_1 and \mathbf{x}_2 follow lognormal distribution with parameters (μ, η) , i.e., $x_{1i} \sim p_L(x; \mu_1, \eta_1)$ and $x_{2i} \sim p_L(x; \mu_2, \eta_2)$, $i = 1, \dots, k_0$. The hypothesis test for patch similarity can be described as $\mathcal{H}_0: \eta_1^2 = \eta_2^2 = \eta^2$ against $\mathcal{H}_1: \eta_1^2 \neq \eta_2^2$. The joint likelihood function for the parameters becomes

$$L(\mu_1, \mu_2, \eta_1, \eta_2) = \left(\frac{1}{2\pi\eta_1\eta_2} \right)^{k_0} \frac{1}{\prod_{i=1}^{k_0} x_{1i}x_{2i}} \times \exp \left[-\frac{1}{2\eta_1^2} \sum_{i=1}^{k_0} (\ln x_{1i} - \mu_1) - \frac{1}{2\eta_2^2} \sum_{i=1}^{k_0} (\ln x_{2i} - \mu_2) \right] \quad (38)$$

and under \mathcal{H}_0 , we obtain

$$L(\mu_1, \mu_2, \eta) = \left(\frac{1}{2\pi\eta^2} \right)^{k_0} \frac{1}{\prod_{i=1}^{k_0} x_{1i}x_{2i}} \times \exp \left[-\frac{1}{2\eta^2} \left(\sum_{i=1}^{k_0} (\ln x_{1i} - \mu_1) + \sum_{i=1}^{k_0} (\ln x_{2i} - \mu_2) \right) \right]. \quad (39)$$

For the lognormal distribution, the MLEs of parameters are given by

$$\hat{\mu}_1 = \frac{1}{k_0} \sum_{i=1}^{k_0} \ln x_{1i} \quad \hat{\mu}_2 = \frac{1}{k_0} \sum_{i=1}^{k_0} \ln x_{2i} \quad (40)$$

$$\hat{\eta}_1^2 = \frac{1}{k_0} \sum_{i=1}^{k_0} (\ln x_{1i} - \hat{\mu}_1)^2 \quad \hat{\eta}_2^2 = \frac{1}{k_0} \sum_{i=1}^{k_0} (\ln x_{2i} - \hat{\mu}_2)^2. \quad (41)$$

By substituting (40) into (39) and taking the partial derivative of the likelihood with respect to η and setting it equal to zero, we obtain the MLE of η as follows:

$$\hat{\eta}^2 = \frac{\hat{\eta}_1^2 + \hat{\eta}_2^2}{2}. \quad (42)$$

Therefore, the GLR becomes

$$\Lambda_L(\mathbf{x}_1, \mathbf{x}_2) = \frac{(\hat{\eta}_1^2)^{k_0/2} (\hat{\eta}_2^2)^{k_0/2}}{(\hat{\eta}^2)^{k_0}}. \quad (43)$$

C) Weibull Distribution: When the amplitudes of scatterers in two SAR patches \mathbf{x}_1 and \mathbf{x}_2 follow Weibull distribution with parameters (μ, η) , i.e., $x_{1i} \sim p_W(x; \mu_1, \eta_1)$ and $x_{2i} \sim p_W(x; \mu_2, \eta_2)$, $i = 1, \dots, k_0$. The hypothesis test for patch similarity can be described as $\mathcal{H}_0: \eta_1^2 = \eta_2^2 = \eta^2$ against $\mathcal{H}_1: \eta_1^2 \neq \eta_2^2$. The joint likelihood function for the parameters becomes

$$L(\mu_1, \mu_2, \eta_1, \eta_2) = \left(\frac{\mu_1\mu_2}{\eta_1\eta_2} \right)^{k_0} \left(\prod_{i=1}^{k_0} x_{1i} \right)^{\mu_1-1} \times \left(\prod_{i=1}^{k_0} x_{2i} \right)^{\mu_2-1} \exp \left[-\frac{1}{\eta_1} \sum_{i=1}^{k_0} x_{1i}^{\mu_1} - \frac{1}{\eta_2} \sum_{i=1}^{k_0} x_{2i}^{\mu_2} \right]. \quad (44)$$

Under the hypothesis $\eta_1^2 = \eta_2^2 = \eta^2$, we have

$$L(\mu_1, \mu_2, \eta) = \left(\frac{\mu_1\mu_2}{\eta^2} \right)^{k_0} \left(\prod_{i=1}^{k_0} x_{1i} \right)^{\mu_1-1} \left(\prod_{i=1}^{k_0} x_{2i} \right)^{\mu_2-1} \times \exp \left[-\frac{1}{\eta} \left(\sum_{i=1}^{k_0} x_{1i}^{\mu_1} + \sum_{i=1}^{k_0} x_{2i}^{\mu_2} \right) \right]. \quad (45)$$

The MLEs of parameters μ_1 and μ_2 are obtained from the following [38]:

$$\begin{cases} \frac{\sum_{i=1}^{k_0} x_{1i}^{\hat{\mu}_1} \ln(x_{1i})}{\sum_{i=1}^{k_0} x_{1i}^{\hat{\mu}_1}} - \frac{1}{\hat{\mu}_1} = \frac{\sum_{i=1}^{k_0} \ln(x_{1i})}{k_0} \\ \frac{\sum_{i=1}^{k_0} x_{2i}^{\hat{\mu}_2} \ln(x_{2i})}{\sum_{i=1}^{k_0} x_{2i}^{\hat{\mu}_2}} - \frac{1}{\hat{\mu}_2} = \frac{\sum_{i=1}^{k_0} \ln(x_{2i})}{k_0} \end{cases} \quad (46)$$

and the MLEs of η_1 and η_2 are given by

$$\hat{\eta}_1 = \frac{1}{k_0} \sum_{i=1}^{k_0} x_{1i}^{\hat{\mu}_1}; \quad \hat{\eta}_2 = \frac{1}{k_0} \sum_{i=1}^{k_0} x_{2i}^{\hat{\mu}_2}. \quad (47)$$

Taking the partial derivative of the likelihood with respect to η , we get the MLE of η for Weibull distribution as follows:

$$\hat{\eta}^2 = \frac{\hat{\eta}_1^2 + \hat{\eta}_2^2}{2}. \quad (48)$$

The GLR under Weibull distribution is then given by

$$\Lambda_W(\mathbf{x}_1, \mathbf{x}_2) = \frac{(\hat{\eta}_1)^{k_0} (\hat{\eta}_2)^{k_0}}{(\hat{\eta})^{2k_0}}. \quad (49)$$

D) K Distribution: The K distribution provides a promising model for SAR amplitude statistics due to its reasonable justification in terms of physical scattering processes [31]. The pdf of K distribution with the shape parameter μ and scale parameter η is expressed as

$$p_K(x; \mu, \eta) = \frac{2}{\eta\Gamma(\mu+1)} \left(\frac{x}{2\eta} \right)^{\mu+1} K_\mu \left(\frac{x}{\eta} \right) \quad (50)$$

where $\Gamma(\cdot)$ is the standard gamma function, and $K_\mu(\cdot)$ is the modified Bessel function of order $\mu > -1$. When the amplitudes of scatterers in two SAR patches \mathbf{x}_1 and \mathbf{x}_2 follow K distribution with parameters (μ, η) , i.e., $x_{1i} \sim p_K(x; \mu_1, \eta_1)$ and $x_{2i} \sim p_K(x; \mu_2, \eta_2)$, $i = 1, \dots, k_0$, we wish to test the hypothesis $\mathcal{H}_0: \eta_1^2 = \eta_2^2 = \eta^2$ with the equal shape parameters against $\mathcal{H}_1: \eta_1^2 \neq \eta_2^2$. The joint likelihood function of the K distribution based on two SAR patches is given by

$$L(\mu_1, \mu_2, \eta_1, \eta_2) = \left[\frac{2}{\eta_1\Gamma(\mu_1+1)} \right]^{k_0} \left[\frac{2}{\eta_2\Gamma(\mu_2+1)} \right]^{k_0} \times \left(\frac{\prod_{i=1}^{k_0} x_{1i}}{2^{k_0}\eta_1^{k_0}} \right)^{\mu_1+1} \left(\frac{\prod_{i=1}^{k_0} x_{2i}}{2^{k_0}\eta_2^{k_0}} \right)^{\mu_2+1} \times \prod_{i=1}^{k_0} K_{\mu_1} \left(\frac{x_{1i}}{\eta_1} \right) \prod_{i=1}^{k_0} K_{\mu_2} \left(\frac{x_{2i}}{\eta_2} \right) \quad (51)$$

$$\Lambda_K(\mathbf{x}_1, \mathbf{x}_2) = \left[\frac{\hat{\eta}_1 \hat{\eta}_2 \Gamma(\hat{\mu}_1 + 1) \Gamma(\hat{\mu}_2 + 1)}{\hat{\eta}^2 \Gamma(\hat{\mu} + 1)^2} \right]^{k_0} \times \frac{\exp \left\{ (\Psi(\hat{\mu} + 1) - \gamma) (\hat{\mu} + 0.5) k_0 - \frac{4k_0 \Gamma(1.5) \Gamma(\hat{\mu} + 1.5)}{\Gamma(\hat{\mu} + 1)} \right\}}{\exp \left\{ (\Psi(\hat{\mu}_1 + 1) - \gamma) \left(\frac{\hat{\mu}_1}{2} + \frac{1}{4} \right) k_0 + (\Psi(\hat{\mu}_2 + 1) - \gamma) \left(\frac{\hat{\mu}_2}{2} + \frac{1}{4} \right) k_0 - 2k_0 \Gamma(1.5) \left[\frac{\Gamma(\hat{\mu}_1 + 1.5)}{\Gamma(\hat{\mu}_1 + 1)} + \frac{\Gamma(\hat{\mu}_2 + 1.5)}{\Gamma(\hat{\mu}_2 + 1)} \right] \right\}} \quad (58)$$

and under the hypothesis $\eta_1^2 = \eta_2^2 = \eta^2$ and $\mu_1 = \mu_2 = \mu$, we have

$$L(\mu, \eta) = \left[\frac{2}{\eta \Gamma(\mu + 1)} \right]^{2k_0} \left(\frac{\prod_{i=1}^{k_0} x_{1i}}{2^{k_0} \eta^{k_0}} \right)^{\mu+1} \times \left(\frac{\prod_{i=1}^{k_0} x_{2i}}{2^{k_0} \eta^{k_0}} \right)^{\mu+1} \prod_{i=1}^{k_0} K_\mu \left(\frac{x_{1i}}{\eta} \right) \prod_{i=1}^{k_0} K_\mu \left(\frac{x_{2i}}{\eta} \right). \quad (52)$$

For K distribution, the MLEs of scale parameters are given by [39]

$$\hat{\eta}_j = \frac{1}{2} \exp \left[\frac{\gamma - \Psi(\hat{\mu}_j + 1)}{2} + \frac{1}{k_0} \sum_{i=1}^{k_0} \ln(x_{ji}) \right], \quad j = 1, 2 \quad (53)$$

where $\gamma = 0.5772$ is Euler's constant, and $\Psi(\cdot)$ is the digamma function. Using a relation between the estimate of the shape parameter and the estimate of the scalar parameters [39]

$$\hat{\eta}_j^k = \frac{1}{2} \left[\frac{\Gamma(\hat{\mu}_j + 1)}{\Gamma(0.5k + 1) \Gamma(\hat{\mu}_j + 1 + 0.5k)} \frac{1}{k_0} \sum_{i=1}^{k_0} x_{ji}^k \right], \quad j = 1, 2 \quad (54)$$

we can estimate the shape parameter $\hat{\mu}_j$ that was found in [39]. For the parameters of likelihood function in (52), similarly, we have

$$\hat{\eta} = \frac{1}{2} \exp \left[\frac{\gamma - \Psi(\hat{\mu} + 1)}{2} + \frac{1}{2k_0} \sum_{i=1}^{k_0} (\ln(x_{1i}) + \ln(x_{2i})) \right] \quad (55)$$

$$\hat{\eta}^k = \frac{1}{2} \left[\frac{\Gamma(\hat{\mu} + 1)}{\Gamma(0.5k + 1) \Gamma(\hat{\mu} + 1 + 0.5k)} \frac{1}{2k_0} \sum_{i=1}^{k_0} (x_{1i}^k + x_{2i}^k) \right]. \quad (56)$$

The estimate of $\hat{\mu}$ can be obtained by combining (55) and (56). It is noted that it is difficult to derive a closed-form expression for GLR in the presence of the modified Bessel function of the second kind in joint likelihood functions. Here, a well-approximated $K_\mu(\cdot)$ is used for a large argument [40], i.e.,

$$K_\mu \left(\frac{x}{\eta} \right) \approx \sqrt{\frac{\pi \eta}{2x}} e^{-\frac{x}{\eta}}, \quad x \gg \eta \quad (57)$$

By taking the first-order moment of the K distribution, i.e., $k = 1$, and substituting (53)–(57) into (51) and (52), we have (58), shown at the top of the page.

REFERENCES

- [1] N. Tomiyama, K. Koike, and M. Omura, "Detection of topographic changes associated with volcanic activities of Mt. Hoshho using D-InSAR," *Adv. Space Sci.*, vol. 33, no. 3, pp. 279–283, 2004.
- [2] D. Sandwell, D. Myer, R. Mellors, and M. Shimada, "Accuracy and resolution of ALOS interferometry: Vector deformation maps of the father's day intrusion at Kilauea," *IEEE Trans. Geosci. Remote Sens.*, vol. 46, no. 11, pp. 3524–3534, Nov. 2008.
- [3] M. E. Pritchard and M. Simons, "A satellite geodetic survey of largescale deformation of volcanic centres in the central Andes," *Nature*, vol. 418, no. 6894, pp. 167–171, Jul. 2002.
- [4] M. Simons, Y. Fialko, and L. Rivera, "Coseismic deformation from the 1999 Mw 7.1 Hector Mine, California, earthquake as inferred from InSAR and GPS observations," *Bull. Seismol. Soc. Amer.*, vol. 92, no. 4, pp. 1390–1402, May 2002.
- [5] Y. Fialko, D. Sandwell, M. Simons, and P. Rosen, "Three-dimensional deformation caused by the Bam, Iran, earthquake and the origin of shallow slip deficit," *Nature*, vol. 435, no. 7040, pp. 295–299, May 2005.
- [6] H. Rotta and T. Naglerb, "The contribution of radar interferometry to the assessment of landslide hazards," *Adv. Space Sci.*, vol. 37, no. 4, pp. 710–719, 2006.
- [7] P. A. Rosen, S. Hensley, I. R. Joughin, F. K. Li, S. N. Madsen, E. Rodriguez, and R. M. Goldstein, "Synthetic aperture radar interferometry," *Proc. IEEE*, vol. 88, no. 3, pp. 333–382, Mar. 2000.
- [8] J. J. Mohr, N. Reeh, and S. N. Madsen, "Three-dimensional glacial flowland surface elevation measured with radar interferometry," *Nature*, vol. 391, no. 6664, pp. 273–276, Jan. 1998.
- [9] T. H. Dixon, F. Amelung, A. Ferretti *et al.*, "Subsidence and flooding in New Orleans," *Nature*, vol. 441, no. 7093, pp. 587–588, Jun. 2006.
- [10] A. Gabriel, R. M. Goldstein, and H. A. Zebker, "Mapping small elevation changes over large areas: Differential radar interferometry," *J. Geophys. Res.*, vol. 94, no. B7, pp. 9183–9191, Jul. 1989.
- [11] A. Ferretti, C. Prati, and F. Rocca, "Permanent scatterers in SAR interferometry," *IEEE Trans. Geosci. Remote Sens.*, vol. 39, no. 1, pp. 8–20, Jan. 2001.
- [12] A. Ferretti, C. Prati, and F. Rocca, "Nonlinear subsidence rate estimation using the permanent scatterers in differential SAR interferometry," *IEEE Trans. Geosci. Remote Sens.*, vol. 38, no. 5, pp. 2202–2212, Sep. 2000.
- [13] G. Fornaro, D. Reale, and F. Serafino, "Four-dimensional SAR imaging for height estimation and monitoring of single and double scatterers," *IEEE Trans. Geosci. Remote Sens.*, vol. 47, no. 1, pp. 224–237, Jan. 2009.
- [14] P. Berardino, G. Fornaro, R. Lanari, and E. Sansosti, "A new algorithm for surface deformation monitoring based on small baseline differential SAR interferograms," *IEEE Trans. Geosci. Remote Sens.*, vol. 40, no. 11, pp. 2375–2383, Nov. 2002.
- [15] R. Lanari, G. De Natale, P. Berardino, E. Sansosti, G. P. Ricciardi, S. Borgstrom, P. Capuano, F. Pingue, and C. Troise, "Evidence for a peculiar style of ground deformation inferred at Vesuvius volcano," *Geophys. Res. Lett.*, vol. 29, no. 9, pp. 6-1–6-4, May 2002.
- [16] P. Lundgren, F. Casu, M. Manzo, A. Pepe, P. Berardino, E. Sansosti, and R. Lanari, "Gravity and magma induced spreading of Mount Etna volcano revealed by satellite radar interferometry," *Geophys. Res. Lett.*, vol. 31, no. 4, pp. L04602-1–L04602-4, Feb. 2004.
- [17] R. Lanari, F. Casu, M. Manzo, G. Zeni, P. Berardino, M. Manunta, and A. Pepe, "An overview of the small baseline subset algorithm: A DInSAR technique for surface deformation analysis," *Pure Appl. Geophys.*, vol. 164, no. 4, pp. 637–661, Apr. 2007.
- [18] A. Hooper, "A multi-temporal InSAR method incorporating both persistent scatterer and small baseline approaches," *Geophys. Res. Lett.*, vol. 35, no. 16, pp. L16302-1–L16302-5, Aug. 2008.
- [19] A. Ferretti, A. Fumagalli, F. Novali, C. Prati, F. Rocca, and A. Rucci, "A new algorithm for processing interferometric data-stacks: SqueeSAR," *IEEE Trans. Geosci. Remote Sens.*, vol. 49, no. 9, pp. 3460–3470, Sep. 2011.
- [20] Z. Li, Z. Bao, H. Li, and G. Liao, "Image autocoregistration and InSAR interferogram estimation using joint subspace projection," *IEEE Trans. Geosci. Remote Sens.*, vol. 44, no. 2, pp. 288–297, Feb. 2006.

- [21] C. A. Deledalle, L. Denis, and F. Tupin, "NL-InSAR: Nonlocal interferogram estimation," *IEEE Trans. Geosci. Remote Sens.*, vol. 49, no. 4, pp. 1441–1452, Apr. 2011.
- [22] J. Chen, Y. Chen, W. An, Y. Cui, and J. Yang, "Nonlocal filtering for polarimetric SAR data: A pretest approach," *IEEE Trans. Geosci. Remote Sens.*, vol. 49, no. 5, pp. 1744–1754, May 2011.
- [23] X. Lv, B. Yazici, V. Bennett, M. Zeghal, and T. Abdoun, "Joint pixels InSAR for health assessment of levees in New Orleans," in *Proc. Geo-Congr.*, San Diego, CA, USA, Mar. 2013, pp. 279–288.
- [24] F. Lombardini, M. Montanari, and F. Gini, "Reflectivity estimation for multibaseline interferometric radar imaging of layover extended sources," *IEEE Trans. Signal Process.*, vol. 51, no. 6, pp. 1508–1519, Jun. 2003.
- [25] R. Bamler and P. Harti, "Synthetic aperture radar interferometry," *Inverse Probl.*, vol. 14, no. 4, pp. R1–R54, 1998.
- [26] A. Kolmogoroff, "Confidence limits for an unknown distribution function," *Ann. Math. Stat.*, vol. 12, no. 4, pp. 461–463, Dec. 1941.
- [27] E. V. Khmaladze, "Goodness of fit problem and scanning innovation martingales," *Ann. Math. Statist.*, vol. 21, no. 2, pp. 798–829, Jun. 1993.
- [28] J. A. Peacock, "Two-dimensional goodness-of-fit testing in astronomy," *Mon. Not. R. Astronom. Soc.*, vol. 202, pp. 615–627, Feb. 1983.
- [29] C. A. Deledalle, L. Denis, and F. Tupin, "How to compare noisy patches? Patch similarity beyond Gaussian noise," *Int. J. Comput. Vis.*, vol. 99, no. 1, pp. 86–102, Aug. 2012.
- [30] J. A. Baglivo, "Mathematical laboratories for mathematical statistics: Emphasizing simulation and computer intensive methods," in *ASA-SIAM Series on Statistics and Applied Probability*. Philadelphia, PA, USA: SIAM, 2005.
- [31] I. R. Joughin, D. B. Percival, and D. P. Winebrenner, "Maximum likelihood estimation of K distribution parameters for SAR data," *IEEE Trans. Geosci. Remote Sens.*, vol. 31, no. 5, pp. 989–999, Sep. 1993.
- [32] J. K. Jao, "Amplitude distribution of composite terrain radar clutter and the K-distribution," *IEEE Trans. Antennas Propag.*, vol. AP-32, no. 10, pp. 1049–1062, Oct. 1984.
- [33] I. S. Reed, J. D. Mallett, and L. E. Brennan, "Rapid convergence rate in adaptive arrays," *IEEE Trans. Aerosp. Electron. Syst.*, vol. AES-10, no. 6, pp. 853–863, Nov. 1974.
- [34] A. M. Guarnieri and S. Tebaldini, "On the exploitation of target statistics for SAR interferometry applications," *IEEE Trans. Geosci. Remote Sens.*, vol. 46, no. 11, pp. 3436–3443, Nov. 2008.
- [35] A. Hooper, "Persistent scatterer radar interferometry for crustal deformation studies and modeling of volcanic deformation," Ph.D. dissertation, Stanford University, Stanford, CA, USA, 2006.
- [36] C. Colesanti, A. Ferretti, F. Novali, C. Prati, and F. Rocca, "SAR monitoring of progressive and seasonal ground deformation using the permanent scatterers technique," *IEEE Trans. Geosci. Remote Sens.*, vol. 41, no. 7, pp. 1685–1701, Jul. 2003.
- [37] A. Parizzi and R. Brcic, "Adaptive InSAR stack multilooking exploiting amplitude statistics a comparison between different techniques and practical results," *IEEE Geosci. Remote Sens. Lett.*, vol. 8, no. 3, pp. 441–445, May 2011.
- [38] K. Rajalakshmi Menon, N. Balakrishnan, M. Janakiraman, and K. Ramchand, "Characterization of fluctuation statistics of radar clutter for Indian terrain," *IEEE Trans. Geosci. Remote Sens.*, vol. 33, no. 2, pp. 317–324, Mar. 1995.
- [39] D. R. Iskander, A. M. Zoubir, and B. Boashash, "A method for estimating the parameters of the K distribution," *IEEE Trans. Signal Process.*, vol. 47, no. 4, pp. 1147–1151, Apr. 1999.
- [40] P. Kasperkovitz, "Asymptotic approximations for modified Bessel functions," *J. Math. Phys.*, vol. 21, no. 1, pp. 6–13, Jan. 1980.



Xiaolei Lv (M'09) received the B.S. degree in computer science and technology and the Ph.D. degree in signal processing from Xidian University, Xi'an, China, in 2004 and 2009, respectively.

From 2009 to 2010, he was with the School of Electrical and Electronic Engineering, Nanyang Technological University, Singapore. From 2011 to 2013, he was with the Department of Civil and Environmental Engineering, Rensselaer Polytechnic Institute, Troy, NY, USA. Since April 2013, he has been with the Institute of Electronics, Chinese

Academy of Sciences, Beijing, China. His main research interests include sparse signal processing, radar imaging (SAR/inverse SAR), interferometric SAR, and ground moving-target indication.



Birsen Yazici received the B.S. degree in electrical engineering and mathematics from Bogazici University, Istanbul, Turkey, in 1988 and the M.S. and Ph.D. degrees in mathematics and electrical engineering from Purdue University, West Lafayette, IN, USA, in 1990 and 1994, respectively.

From September 1994 to 2000, she was a Research Engineer with the General Electric Company Global Research Center, Schenectady, NY, USA. During her tenure in industry, she worked on radar, transportation, industrial, and medical imaging systems. From

2001 to June 2003, she was an Assistant Professor with the Department of Electrical and Computer Engineering, Drexel University, Philadelphia, PA, USA. Since 2003, she has been with Rensselaer Polytechnic Institute, Troy, NY, USA, where she is currently a Full Professor with the Department of Electrical, Computer, and Systems Engineering and the Department of Biomedical Engineering. She is a holder of 11 U.S. patents. Her research interests include statistical signal processing, inverse problems in imaging, image reconstruction, biomedical optics, and radar and X-ray imaging.

Dr. Yazici was an Associate Editor for the IEEE TRANSACTIONS ON IMAGE PROCESSING from 2008 to 2012. She currently serves as an Associate Editor for the *SIAM Journal on Imaging Science*. She was the recipient of the Rensselaer Polytechnic Institute School of Engineering Research Excellence Award in 2007 and 2013.



Mourad Zeghal received the B.S. and Ph.D. degrees from Tunis University, Tunis, Tunisia, in 1983, and Princeton University, Princeton, NJ, USA, in 1990, all in civil engineering.

He is currently an Associate Professor with the Department of Civil and Environmental Engineering, Rensselaer Polytechnic Institute, Troy, NY, USA. He is active with the Center for Network for Earthquake Engineering Simulation, Scientific Computation Research Center, and the Inverse Problems Center.

His research interests include computational soil micromechanics, geotechnical system identification, seismic response monitoring, and information technology applications in geomechanics.



Victoria Bennett received the B.S., M.E., and Ph.D. degrees from Rensselaer Polytechnic Institute (RPI), Troy, NY, USA, all in geotechnical engineering.

She is currently an Assistant Professor with the Department of Civil and Environmental Engineering, RPI. Her main research interests include geotechnical field instrumentation and monitoring, and the applications of radar remote sensing for long-term ground surface monitoring.



Tarek Abdoun received the B.S. degree in civil engineering from Cairo University, Giza, Egypt, in 1991 and the Ph.D. degree in geotechnical engineering from Rensselaer Polytechnic Institute (RPI), Troy, NY, USA, in 1997.

Since 1998, he has been with the Department of Civil and Environmental engineering, RPI. He is also currently the Associate Dean for Research and Graduate Studies and the Technical Director of the NEES Geo-Centrifuge Center. He is the author of over 160 published technical papers and research

reports. His main research interests include physical modeling, field testing, field monitoring, and earthquake engineering.

Dr. Abdoun received several national and international awards, including the American Society of Civil Engineers Walter L. Huber Award and the U.S. Army Commander's Award and Medal.